Fabrication with magnetic-spin coating: influence of magnetic-inertia energy ratio on gold-pickering ferrofluid droplet assembly morphology.

OKPOZO, P., NJUGUNA, J., ISLAM, S., UYANGA, K. and PANCHOLI, K.

2024

Journal of Magnetism and Magnetic Materials 611 (2024) 172577

Contents lists available at ScienceDirect

Journal of Magnetism and Magnetic Materials

journal homepage: www.elsevier.com/locate/jmmm

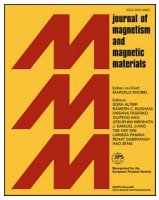

Research article

Fabrication with magnetic-spin coating: Influence of magnetic-inertia energy ratio on gold-pickering ferrofluid droplet assembly morphology

Paul Okpozo [a,*], James Njuguna [a,b], Sheikh Islam [a], Kindness Uyanga [c], Ketan Pancholi [a,*]

[a] School of Engineering, Sir Ian Wood Building, Robert Gordon University, Garthdee, Aberdeen AB10 7GJ, UK
[b] National Subsea Centre, 3 International Ave., Dyce, Aberdeen AB21 0BH, UK
[c] Department of Mechanical Engineering, City University of Hong Kong, 83 Tat Chee, Avenue, Kowloon, Hong Kong

ARTICLE INFO

Keywords:
Spin coating
Magnetism
Chain thickness
Chain gap
Energy ratio
Pickering emulsion

ABSTRACT

Magnetic self-assembly of nanoparticles is a well-known technique for creating thin-film array-patterned functional microstructures. However, an uncontrollable hierarchical assembly formation of magnetically stimulated particles has hindered the desired formation of free-standing two-dimensional (2D) array patterns in thin-film layers. In this study, we proposed a fluidic shearing effect from spin coating to reduce the magnetically stimulated particles' disarrayed and complex chain formations. This would thus promote linear array formations, even as the film becomes thinner. A series of tests were conducted on a gold-pickering ferrofluid emulsion (GPFE) dispersed in 15.2 mPas aqueous polyvinyl alcohol (PVAh) under varying spin speeds and magnetic setups such as single (SI), compound (CC), and concentric (CR). These setups were chosen to observe the influence of magnetic field strength and distribution on the generated pattern profile from microscopic binary images of the resulting thin films. The aim was to quantify the formed chain thickness (ChT), chain gaps (ChG), and chain lengths (ChL) to capture the morphology and geometrical features of the formed patterns. Our results showed that the quantified values of these profiles and their dimensionless relationships were significantly influenced by the ratio between the applied magnetic packing energy and the centrifugally controlled fluidic energy, Q_{PD}. This investigation showed that ChT/ChG for a corresponding Q_{PD} value is 98.6% the same for all configurations, and CR was the best setup going forward, as it yielded the lowest array quality defectivity of 14%. Therefore, we assert that this fabrication method offers flexibility, cost-effectiveness, and expandability in generating linear array patterns that contain graduating variability in grating order dimensions within a single cast that can serve efficiently as a substrate for biomolecules under enhanced Raman and Infrared spectroscopies.

1. Introduction

Magnetic manipulation of particles is a phenomenon where materials that respond to magnetic fields are aligned in response to the force and direction of an existing magnetic field. The method is known as magnetic-stimulated self-assembly, which is a non-intrusive, fast, cost-effective, and orientational means of forming linear array patterns [1–3]. However, the effectiveness of this stimulation is primarily achieved using magnetically responsive materials, including paramagnetic, ferromagnetic, ferrimagnetic, and diamagnetic materials [4,5]. Ferrimagnetic materials, when exposed to a magnetic field, tend to form a chain-like particle structure with a 'head-to-tail' dipole–dipole configuration due to their crystal structure. These materials also exhibit perpendicular repulsion between particles with opposing alignment, leading to the creation of linear arrays of chain structures. As the angle between opposing particles decreases from 90 degrees to approximately 54 degrees, the repulsion between them decreases [3]. Ferrimagnetic particles possess a unique magnetism characteristic that has been used for stimulated-directed self-assembly (SDSA) techniques to create sub-micron/micron scale patterns. Linear array patterns formed through SDSA allow for the diffraction of electromagnetic waves or the slowing down of different wavebands of the electromagnetic wave, which is similar to the grating order of SDSA array formation. Other researchers have conducted and reported on the manipulation of electromagnetic waves, such as photonic band gaps, using magnetic methods [3,6,7]. The changes in bandgap depend on the intensity of the magnetic field applied. These changes in bandgap play a crucial role in the development of structures for opto-conversion applications, particularly for

* Corresponding authors.
E-mail addresses: p.okpozo@rgu.ac.uk (P. Okpozo), k.pancholi2@rgu.ac.uk (K. Pancholi).

https://doi.org/10.1016/j.jmmm.2024.172577
Received 16 August 2024; Received in revised form 29 September 2024; Accepted 3 October 2024
Available online 16 October 2024

materials that have fast decay rates due to electron and hole collisions in the case of semiconductors (such as iron oxide) or electron collisions in the case of metals (like gold) [8–10].

It has been observed that applying magnetic stimulation can temporarily alter the linear dipole–dipole and particle–particle patterns. This, in turn, can lead to the formation of complex 3D units [11,12]. This issue is particularly noticeable in situations where the magnetic field is excessively strong in a specific area. Such occurrences have been previously studied in ferrofluids within D2O emulsion systems, with varying strengths of magnetic fields. Studies have been conducted to understand the phenomenon better [13,14]. In comparison to solid magnetic spheres or iron oxide nanoparticles, the ferrofluid droplet containing iron oxide particles is able to move freely and orient itself, allowing it to undergo a combined Neel rotation and Brownian motion. This makes it a suitable material for forming dipole–dipole translational chain order in the study being conducted [15,16]. Its oil-based interface could potentially play a role in picking gold nanoparticles, as studied and executed in a conventional gold-pickering oil/water emulsion system [17–20]. The formation of 3D hierarchical complexes in magnetized droplets can be prevented by introducing a spin-coating (fluidic) method. This generates fluid inertia with shear stress on the droplets and can potentially stretch the structure into linear patterns. Previous attempts to combine the magnetic field and spin coating to prepare a film using a Helmholtz coil system (illustrated in Fig. 1) resulted in a series of more complex 3D hierarchical structures [21–24]. The observed formation is a phenomenon that can be explained by the interaction between the magnetic field direction generated by the Helmholtz coil and the circumferentially driven particles on the spinning substrate. The stationary magnetic flux, the radial vector force caused by the fluid inertia, and the circumferential vector of the spinning substrate work together to create a unique experience for the magnetic particles, which is commonly known as 'Flux Switching' [21,22].

In this study, some modifications were made to their experimental setup by placing a permanent magnet underneath the substrate to immobilize the magnetic colloidal suspension. Then a spin coater was used to coat the substrate surface with colloidal material [25,27]. This arrangement helped eliminate the 'flux switch' problem and reduced it to a two-dimensional force problem involving radial-directional fluid inertia and radial magnetic force gradient. To estimate the extent of the magnetic effect on colloids, a relationship like the ratio of magnetic and other forms of countering forces, such as the Hartmann number, thermal stability number, dipole number, and packing number was considered [26]. This was carried out by analyzing the pattern morphology through optical image analysis, they were able to relatively quantify the impact of the contending forces between the magnetic and inertial forces.

Previous studies have employed image analysis of magnetised colloidal patterns. Such images were pre-processed into grayscale, and the resolution of the chain thicknesses and chain gaps were quantified [11,12]. From such image analysis outcome, in combination with estimated fluidic and magnetic energy ratios (or number), a relational map can hereby be created to observe the influence of physical parameters on structural partterning of Pickering emulsions.

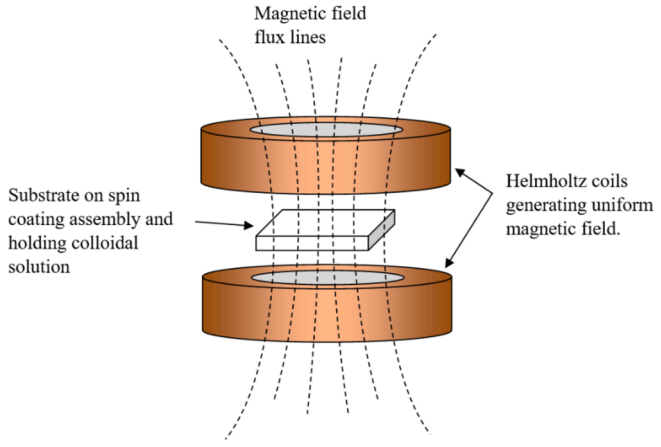

Fig. 1. Illustration of field lines generated by the Helmholtz coil across the spin-rotated substrate.

This study is significant as it identifies an exemplary magnetic configuration and spin speeds that can be utilized to control the production of multi-dimensional micron-patterned structural assembly of ferromagnetic and paramagnetic colloids, which is an advancement from previous SDSA studies [25,27]. This self-assembly technique is quick and cost-effective, making it useful in producing structured surface components for low-end optoelectronic applications such as Surface Enhanced Raman Spectroscopy (SERS) and Surface Enhanced Infrared Absorption (SEIRA), as has been previously conducted [27].

2. Materials and methods

2.1. Materials

Iron powder (fine), *cis*-cyclooctene (Mw 110.2 g/mol), HCL acid (37 % w/w molar concentration), NH_4OH (30 % wt. ammonia in water), H_2O_2 (30 % w/w in water), polyvinyl alcohol (PVA) (Mw 88000 g/mol), oleic acid (Mw 282.46 g/mol), gold (III) chloride (30 wt% HCl – Mw 339.79 g/mol), sodium methacrylate (Mw 108.07 g/mol) and polyethylene glycol 40 stearate (PEG 40S) were purchased from Sigma–Aldrich. De-ionized water (DI) with 18 MΩ resistivity, Whatman glass microfiber filter paper (GF/A), and a a p-type,–boron dopant, <110 > double side polished silicon wafers were purchased from Pi-Kem [28]. They possess properties such as a crystal growth-float zone of–prime grade type with 4 in diameter, and a roughness of less than 2 Å, resistivity of 10,000 Ω-cm, thickness of 525 μm, and flatness (TTV) of less than 1 μm. These were based on Pi-kem web documentation [29]. The silicon wafer was cut into sizes with dimensions 27.5 mm × 40 mm.

2.2. Preparation

To create a thin film of the gold Pickering ferrofluid emulsion (GPFE) in polyvinyl alcohol (PVAh), a method previously reported in the literature [27,28] was employed. This process utilized magnetic and spin coating techniques under the specific conditions outlined in Table 1. Magnetizing the GPFE within the PVAh solution was anticipated to cause the emulsion to migrate towards areas with stronger magnetic fields, thus forming dense dipole–dipole clusters and chains [30]. To facilitate this, a setup was designed as depicted in Fig. 2, with the magnet positioned approximately 5 mm below the substrate surface, providing a cross-sectional view of the arrangement.

The Neodymium permanent magnets configurations were varied, as schematised in Fig. 3, showing;

- A single square (SI) – a 3 mm × 3 mm × 3 mm square Neodymium Magnets.
- A cylinder on cylinder-compound (CC) – consists of a 6 mm diameter, 0.5 mm thick disc-type, and 3 mm diameter, 2 mm thick cylindrical Neodymium Magnet.

Table 1
Sample setup and process parameters at room temperature. The approach determined the density [31].

Weight per cent PVAh	Density (kg/m^3)	Viscosity mPa.s	Surface Tension (mN/m)	Centrifugal speed (rev/min)	Time (sec)
3.3 %	1011	15.2	51.72	2000, 2500, 3000, 3500.	60

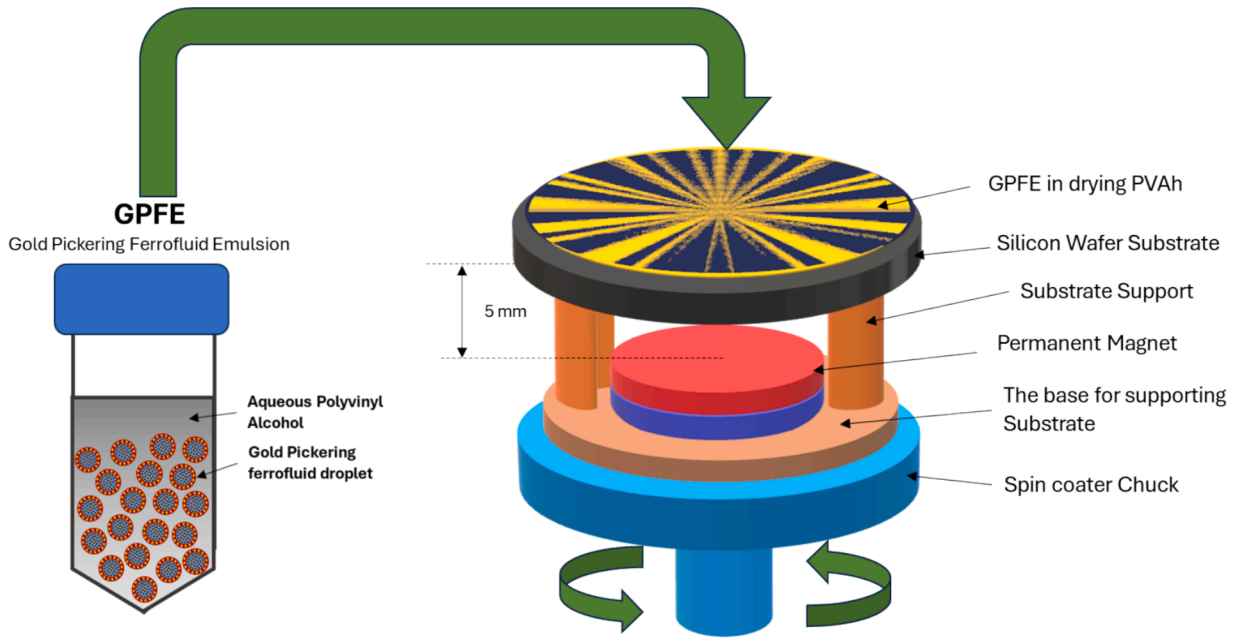

Fig. 2. Schematic of cross-section dimensions of the experimental setup with droplet interaction in the magnetised ferrofluid-polymer emulsion.

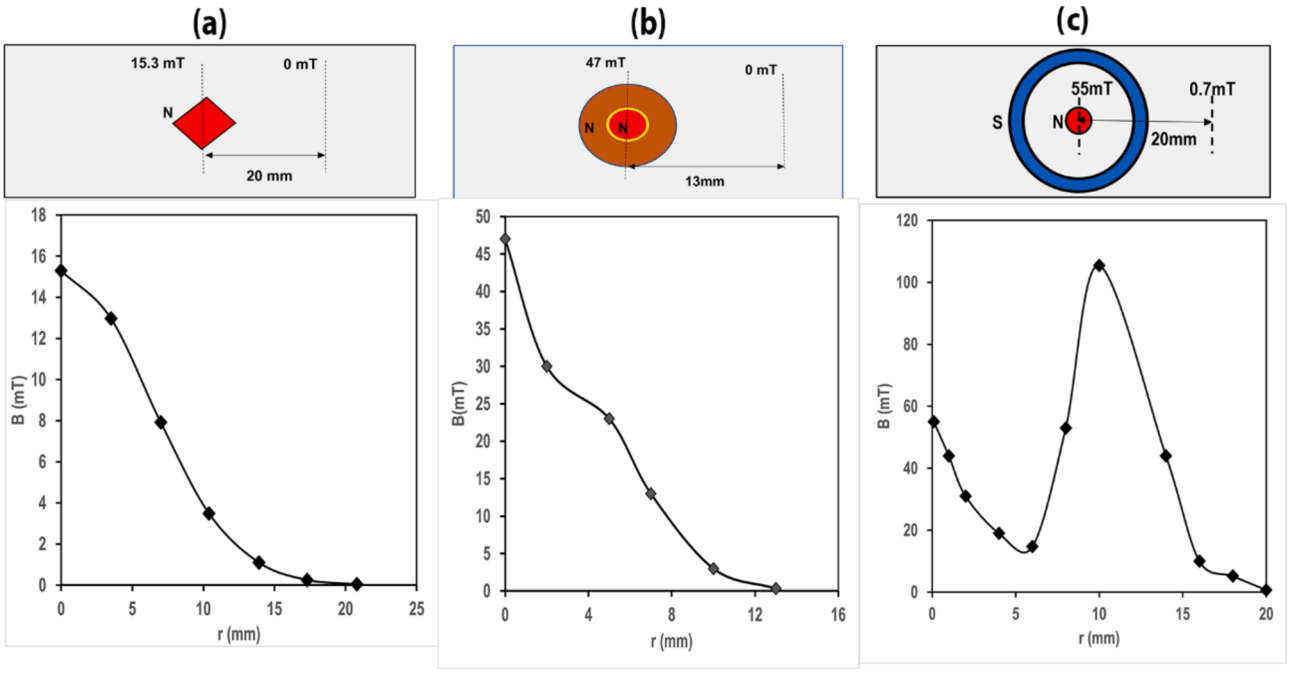

Fig. 3. Permanent magnet configurations and respective average measured magnetic field strength (B mT) profiles along the radius (r mm) (below) for; (a) Single-Square (SI), r = 20 mm (b) Cylinder-Cylinder-Compound (CC), r = 13 mm, and (c) Cylinder-Ring-Concentric (CR), r = 20 mm. The 'N' represents the North pole, and 'S' represents the South pole of the magnet.

- A cylinder-ring-concentric (CR) – a combination of a 3 mm diameter, 2 mm thick cylindrical, and a 25 mm OD, 15 mm ID and 5 mm thick ring-type Neodymium Magnets.

All magnets were purchased from First4magnets® UK. The empty substrate was ground at a resolution of 1 mm. Three radial directions were scanned using a VTSYIQI® probe-type gaussmeter (0 to 2000mT, resolution of 0.1mT, and accuracy of 1 %) to obtain the average radial magnetic field distribution (mT) for each magnetic configuration [28]. These different setups were selected to observe the influence of the combined magnetic field strength and distribution on the pattern profile and geometry. The B (mT) vs. r (mm) profiles in Fig. 3 show the mean magnetic field strength between the middle of the substrate and approximately zero field strength.

The experimental procedure utilised the SCS™ 6800 spin coating series equipment, programmed to operate at variable speeds over a specified duration. The process was divided into three phases: (1) an acceleration phase from 0 rpm to the maximum speed lasting 1 s, (2) a constant maximum speed phase lasting 54 s, and (3) a deceleration phase lasting 5 s. Table 1 details the experimental protocols employed. A slide with an attached magnet was placed on the spin coater's chuck. The substrate support comprised an 8 mm thick machined acrylic layer,

topped with 0.2 mm double-sided adhesive tape. The glass substrate was subsequently affixed to the setup using the same adhesive tape.

GPFE was synthesized in an aqueous PVAh solution (3.3 wt%) following the methodology outlined in [27,28]. To investigate variations in the geometric morphology of the thin film pattern, different spin speeds were employed (as detailed in Table 1). The spin coating process consisted of an acceleration phase to the maximum speed over 1 s, a constant speed phase for 54 s, and a deceleration phase lasting 5 s. The outcomes of these experiments are summarized in Table 1.

Prior to spin coating, 0.5 ml of the GPFE in PVAh solution was deposited onto the substrate and allowed to settle for 60 s. This interval enabled the droplets to interact with the magnetic field and form chain clusters based on prior research by Femigar and Gast [32] and Nowak and Co. [33]. Following 60 s of spinning, the thin film coating was dried. It is critical to achieve sufficiently high spin speeds to ensure adequate evaporation of the water solvent, as both experimental and theoretical evidence confirm that the evaporation rate is directly proportional to the square root of the spin speed and the solute concentration in the solvent [34]. Incomplete drying results in the disassembly of the GPFE droplet clusters upon removal from the setup. Consequently, drying the Pickering emulsion film at high speeds (>700 rpm) is essential to maintain the GPFE array structure within the dried PVAh film post-spin-coating.

2.3. Film analysis procedure

The coated samples were imaged using an Olympus® BX41 Darkfield microscope and subsequently processed into a binary format using Image J®. Image processing involved converting the images to eight bits, enhancing profile sharpness and edges, and increasing contrast by 10 %. Subsequently, binary values were assigned based on pixel intensity, where black was represented as 0 and white as 255, using the plot profile tool [35,36]. This method facilitated clear differentiation of the GPFE droplet assembly profile from the background across the film.

For higher magnification images beyond the tens of micron field of view, a Quanta 650 FEG Scanning Electron Microscope (SEM) was utilized. The SEM operated under a low-pressure vacuum of 0.825 Torr, with an accelerating voltage (HV) of 20 kV, and a consistent working distance of 10 ± 1 μm for all point scans, adjusted according to the required magnification.

Darkfield microscopy images were utilised for chain profile analysis due to their larger field of view and contrast between the Pickering droplets and substrate (background). SEM, on the other hand, provides detail on inter-droplet interaction but has a much lower field of view. Therefore Darkfield microscopy image provides average values of chain profiles across multiple scanned points. This saves time, and results are much more easily estimated.

2.4. Energy ratio relationship

The pattern induced by the combined magnetic and spin-coating processes displays distinct characteristics. Close to the substrate center, the magnetic force predominates over the centrifugal force generated by inertia. Moving outward from the center, centrifugal forces progressively outweigh the magnetic force, as evidenced in the preceding analysis. To understand the influence of these forces on the two-dimensional linear arrangement of particles within the thin film and its overall resolution, a structural resolution map was generated based on dimensionless quantities and ratios.

Key parameters defining the dimensions of linear arrays of metal heterostructures included chain length (ChL), chain thickness (ChT), and array gap (ChG). These parameters were expressed as ratios ChL/ChT and ChT/ChG. The dimensionless approach facilitated a relative assessment of metal heterostructures in linear arrays compared to the traditional grating order. This approach drew inspiration from previous studies that varied the thickness or width of gold strips while maintaining a constant grating order, revealing noticeable changes in absorption wavelengths due to surface plasmons [28,37,38].

In our study, we explore the effects of ChL/ChT and ChT/ChG parameters, which describe how chain length varies relative to chain thickness and array gap, respectively. Higher magnetic field strengths led to the formation of thicker columns or labyrinths, characterized by irregular, closely packed structures that disrupt the uniformity of long dipole–dipole chains. Strong magnetic fields promoted tight aggregation of GPFE droplets with minimal interstitial spacing, whereas weaker magnetic fields resulted in more pronounced gaps between droplets. Consequently, the ratios ChL/ChT and ChT/ChG reflect the balance between magnetic energy and the energy of a fluid on a spinning disc.

The presence of a magnetic field has an impact on the behaviour of GPFE droplets in a mixture that contains different substances. When exposed to a magnetic field, the GPFE droplets tend to come together and form chains or columns on the surface of the substrate. The size and shape of these aggregates depend on the strength of the magnetic field and their location on the substrate. The energy formula that determines the packing of GPFE droplets into aggregates has been studied and established [28,39]:

$$E_{MP} = m_{DD} \bullet B \tag{1}$$

where B is the magnetic field strength in ($kg.A^{-1}.s^{-2}$) at a particular location on the substrate surface and m_{DD} is the droplet dipole moment of interaction ($A.m^2$), given as Eq. (2) [40].

$$m_{DD} = \left(\frac{\pi {d_p}^3}{6}\right)\left(\frac{M_{PD}\mu_o}{B}\right)\left(2\frac{B}{\mu_o} - M_{PD}D_{dm}\right) \tag{2}$$

In this study, d_p represents the droplet diameter, M_{PD} denotes the magnetization ($A\ m^{-1}$) of the Pickering droplets, and μ_o is the free space magnetic permeability, valued at $4\ \pi \times 10^{-7}$ $Henry.m^{-1}$. The demagnetization factor D_{dm} is assumed to be 0.333 due to the spherical shape of the droplets [41]. The equivalent magnetization $M_{PD} = 0.06 \times M(H)$ of a Pickering droplet comprises magnetized magnetite nanoparticles, as depicted in the M(H) curve shown in Supplementary S1.1.

When a cluster of Pickering droplets undergoes spin coating under centrifugal forces, the generated energy deforms the aggregates and disperses the droplets. The magnetic packing energy E_{MP} (as defined in Equation 1) and the fluid inertia energy E_{FI} are characterised as follows [28]:

$$E_{FI} = \frac{1}{2}\rho_{pva} V_{pd} {u_a}^2 \tag{3}$$

where V_{pd} is the volume of the spherical ferrofluid droplet, u_a is the velocity of aqueous PVAh from centrifugal action, ρ_{pva} is the density of aqueous PVAh, and

By definition, the velocity of a thin liquid over a spinning disc is given by Equation [4]:

$$u_a = \frac{\rho_{pva}\omega^2 R h_o^2}{\mu} \tag{4}$$

$$V_{pd} = \frac{\pi d_p^3}{6} \tag{5}$$

$$E_{FI} = \frac{{\rho_{pva}}^3 \omega^4 h_o^4}{\mu^2}\frac{R^2}{2}\frac{\pi {d_p}^3}{6} \tag{6}$$

where ω is the top spin speed (rpm), R is the radial distance from the centre of the spinning substrate, and h_o is the initial liquid height from the surface of the substrate.

To investigate and correlate the influence of energies on the resolution of patterns in a thin film, the energy ratio of E_{MP}/E_{FI} was employed. This ratio assesses the force competition between the driving fluid and the local magnetic dipole–dipole forces, which arise from the shear stress exerted by the fluid between the magnetized droplets.

Assuming the droplets behave as hard spheres, this shear stress may lead to the fragmentation of chain lengths, reduction in chain widths, and an increase in gaps between droplets. To analyze particle displacement, an x, y coordinate system was utilized, with the characteristic chain length measured radially from the center. The liquid inertia was considered to be dependent on the characteristic height of the liquid relative to the substrate surface [28].

The characteristic height used for this study was h_i (m), which is the new film height after t (s) spinning at the top spin speed (ω rpm) from the initial height h_o (m). The h_o was estimated from the optical images shown in Supplementary S.1.3. The density of the PVAh used in this study was 1.011 g/ml (or 1011 kg/m^3), which gave an equivalent film initial height (h_o) of 0.48 mm. Thus, h_i was determined by applying Eq. (7) while ignoring the evaporation rate [42].

$$h_i = h_o / \sqrt{1 + \frac{4\rho_{pva}\omega^2 h_o^2 t}{3\mu}} \tag{7}$$

The thinning of the film following the spin coating model h_i and radial position 'R' after spin time 't' led to the film's boundary condition, which can be represented by the ratio, $E_{CL} = h_i/R$, defined as the thin film parameter [43,44]. When used to divide the ratio, E_{MP}/E_{FI} provides a dimensionless parameter, Q_{PD} ($Q_{PD} = E_{MP}E_{FI}^{-1}E_{CL}^{-1}$). This parameter was plotted against the ChL/ChT and ChT/ChG ratios to develop a pattern resolution map.

3. Results and discussions

The comprehensive characterisation of GPFE can be found in previous works of Okpozo and Co. [25,27]. The size distribution of gold pickering ferrofluid after ultrasonication had bimodal peaks (See Supplementary Information S12). After centrifugal segregation, the size distribution of GPFE reduced to a single peak of 200 ± 30 nm. A sample transmission electron micrograph of gold pickering ferrofluid droplet can be seen in Fig. S11. Employing a combination of magnetic and spin coating techniques, a patterned thin film of GPFE in 3.3 wt% PVAh solution was spun at various rotational speeds. For instance, a sample prepared at 3500 rpm is depicted in Fig. 4(a). Fig. 4(b) shows a microscopic image captured using an Olympus® BX41 brightfield microscope in reflection mode, equipped with a 5 × magnification lens (N.A. 0.1). The samples exhibited a birefringent ring of refracted light, a result of the density and distribution of organized GPFE droplets, consistent with conventional magnetized nanospheres [3]. The dipole–dipole interaction among GPFE droplets under a magnetic field influenced the structuring of diffracting orders of linear chains and gaps, which varied gradient-wise across the thin film. Therefore, the observed changes qualitatively reflect the interplay between applied magnetic and fluid-inertia energies, highlighting the tunability of pattern resolution.

3.1. Energy ratio influence on pattern geometry

The samples utilized in this investigation consisted of a Pickering emulsion dispersed in 3.3 wt% aqueous PVAh. Fig. 5 illustrates a representative profile analysis from images acquired under magnetic influence at spin speeds of 3500 rpm, with radial measurements taken at 1 mm and 3 mm distances from the centre of the substrate. The combination of the aforementioned parameters yielded ratios Q_{PD} = 14.2 and 5.7 for the binary processed images in Fig. 5(a) and (c), respectively. Fig. 5(b) and (d) depict 3D plots of scans conducted at four equidistant locations (designated by red lines B, D, F, and H) separated by approximately 50 μm. Thicker distributions of binary plots were observed in Fig. 5(a), whereas thinner distributions were evident in (c). Due to the challenge in distinguishing complete lines, divisions greater than zero were counted as droplets, while zero values were considered as gaps. The pixel division used for analysis was set at 168 nm per pixel. A brief sample dataset is presented in Supplementary Table S-II, detailing binary values (>0 and 0) across each 168 nm division [28]. However, these values do not accurately represent the physical thickness of the chains and gaps. Consequently, a code was developed (described in Supplementary S.2.1) to categorize consistent divisions of white pixels (>0) and black pixels (0) into counts for chain thickness (CntCT) and chain gaps (CntGap), respectively, as demonstrated in Supplementary Table S-III. The calculated values were scaled by 0.168 μm to derive dimensional estimates for chain thickness and gaps. The average values (Av) from the profile scans were subsequently processed to determine the ratio between chain thickness and the intervening gap using Av/(1-Av), with detailed averages and standard deviations presented in Table 2.

A manual measurement procedure was executed for chain length (green profile lines in Fig. 5(a and c). However, the breakage of the dipole–dipole chain led to variations in the estimated chain lengths following measurements using the condition of chain breakage when the break gap was greater than 1 μ m.

A manual measurement protocol was employed to determine the chain lengths (indicated by green profile lines in Fig. 5(a) and (c)). Variations in estimated chain lengths occurred due to the breakage of dipole–dipole chains, defined as instances where the gap between segments exceeded 1 μm during measurement.

Supplementary Table S-V presents the average chain thickness, chain gap, and chain length for various regions at different spin speeds (2000, 2500, 3000, and 3500 rpm), which is crucial for understanding how pattern distribution responds to spin speed [27]. To derive non-dimensional values and relationships, ratios such as ChT/ChG and ChL/ChT were calculated. The ChT/ChG ratio is particularly significant as it estimates the grating size, allowing observation of how changes in thickness and gap correlate with variations in Q_{PD} values. Moreover, exploring the influence of gold strip grating order and strip thickness on local charge density for infrared-enhanced vibrational detection of analyte molecules underscores the relevance of this dimensionless ratio [36,37]. Overall, this data and analysis are vital for advancing knowledge in this area and will inform future research [36,37]. The ChL/ChT ratio was utilized to assess the effective change between the cross-section and length of dipole chains. As clusters of GPFE droplets formed, the chain thickness increased progressively, resulting in vertical columns with a higher incidence of breakage between chains. Furthermore, at sufficiently high fluid velocities, oriented Pickering droplets were sheared and displaced, leading to breakages in chain length.

Drawing insights from previous studies [10,11], it was elucidated how augmenting the magnetic field strength induces the formation of thicker columns and labyrinthine structures [10,11]. Q_{PD} was computed to discern regions of the substrate and deposited solution experiencing differing levels of energy dominance between magnetic and centrifugal forces. Two logarithmic relationships were established (Fig. 6), correlating ChL/ChT vs. Q_{PD} and ChT/ChG vs. Q_{PD}, with radial points serving as a consistent parameter across each dimensionless ratio.

In the region denoted as A in Fig. 6, where $Q_{PI} < 1$, the values for ChT/ChG and ChL/ChT remain constant. In this domain, the fluid inertia energy exceeds the magnetic energy, resulting in the random dispersion

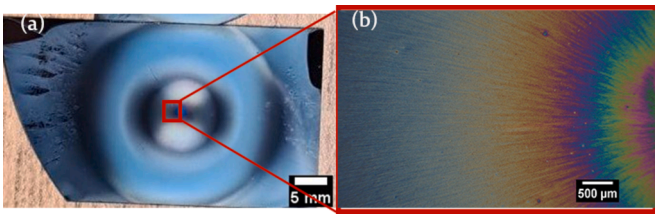

Fig. 4. (a) Magnetic-directed spin coating prepared film on the silicon wafer substrate using the CR magnetic setup. Image (b) Section of film obtained using Olympus brightfield microscope under reflection mode with a 5 × magnification lens, N.A. = 0.1.

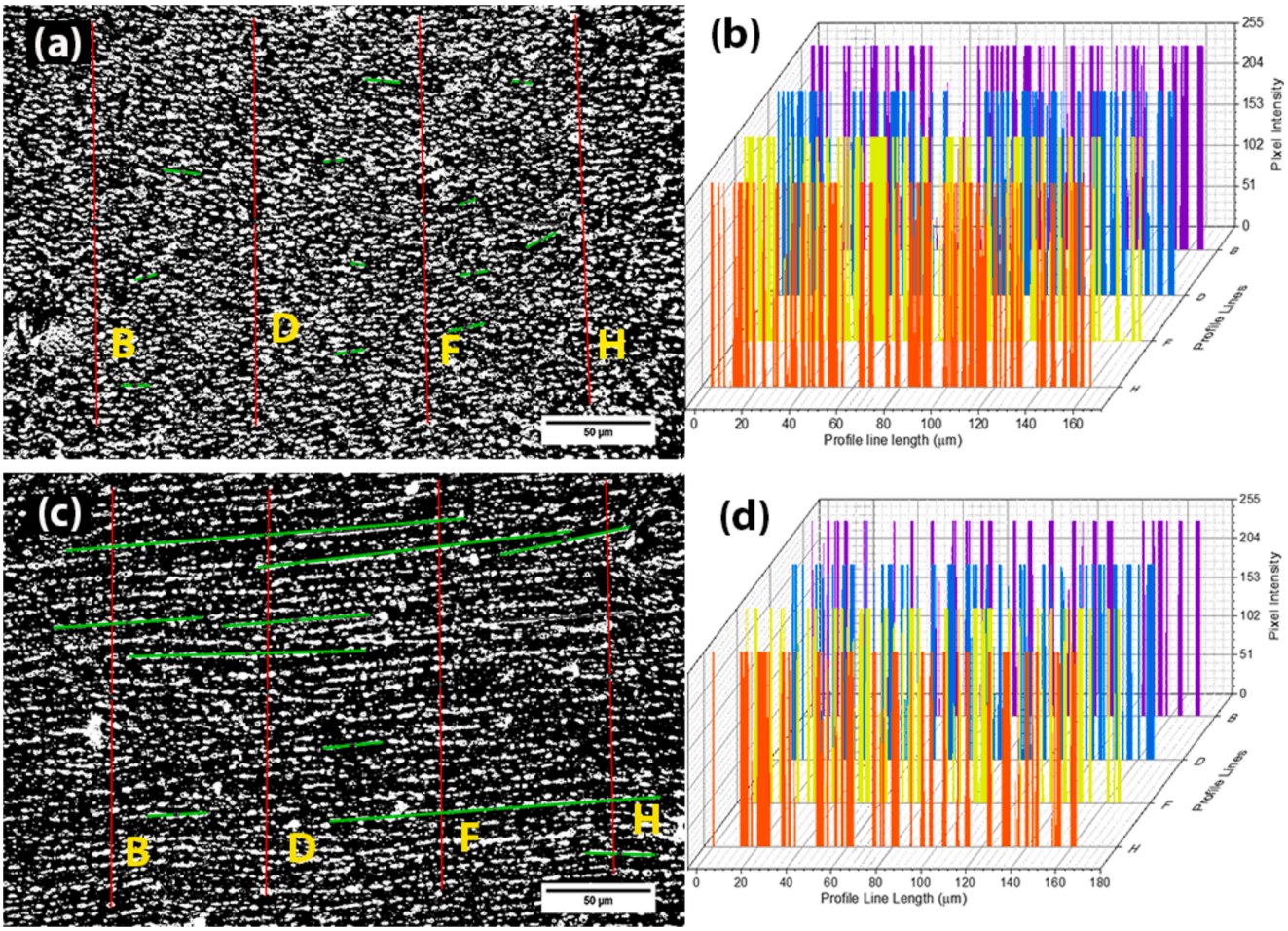

Fig. 5. Average resolution of pitches between chain thickness and gap was determined from region of interest scan profile lines (red lines B, D, F & H) of binary processed plot profile images (a and c). The green lines are manually measured chain lengths. Images (b and d) are generated profile distributions for $Q_{PD} = 14.2$ (a) and $Q_{PD} = 5.73$ (c). (For interpretation of the references to colour in this figure legend, the reader is referred to the web version of this article.)

Table 2
Summary of results obtained from image analysis of a sample prepared with an SI configuration under a 3500 rpm spin speed. *SD-Standard Deviation.*

3500 RPM									
r (m)	**ChG (μm)**	**ChT (μm)**	**ChL (μm)**	**SD-ChG**	**SD-ChT**	**SD-ChL**	**ChL/ChT**	**ChT/ChG**	**Q_{PD}**
0.001	2.32	2.66	42.7	0.14	0.23	5.32	16.05	1.15	13
0.0025	2.65	2.46	93	0.22	0.2	1.72	37.8	0.93	5
0.0042	2.82	2.15	209	0.5	0.07	19.0	97.2	0.73	2
0.0049	3.05	1.94	98	0.58	0.14	13.5	50.5	0.64	1.5
0.0057	5.03	1.215	1.21	0.32	0.076	0.34	1.0	0.24	1

of GPFE droplets due to centrifugal forces. This behaviour is consistent with other magnetic dimensionless numbers such as the Magnet Bond number, Hartman number, Magnetic Laplace number, and thermal stability number, where the competing energy component dominates at ratio values below unity compared to the magnetic energy [25,45–47]. This effect is particularly notable at points further from the centre of the substrate, where the droplet concentration is lower, leading to larger gaps between droplets. Consequently, ChG is greater than the droplet diameter (ChT), as depicted in Fig. 7a. In region A, ChL/ChT values are unity, corresponding to the droplet diameter.

For the energy ratio range ($1 \leq Q_{PD} \leq 10$), regions B and C were analysed for ChL/ChT and ChT/ChG. In region B, an increase in magnetic energy surpassed fluid inertia, indicating a rapid change in chain length compared to chain thickness. The sharp rise from ChL/ChT = 1 to ChL/ChT ~ 100 within the narrow energy ratio range ($1 \leq Q_{PD} \leq 2$) suggests an increasing number of droplet–droplet interactions forming chains (see insert Fig. 7a). This increase was coupled with a gradual rise in chain thickness due to droplet clustering, as ChT/ChG increased from 0.3 to 0.7. However, gaps persisted between the formed chains in region C. At $Q_{PD} = 2$, inertia energy was at least half of the magnetic energy, corresponding to the maximum chain length (from ChL/ChT ~ 100), where ChT/ChG = 0.5 (see Fig. 7b). The growth of thicker chains due to increased magnetic field and lower inertia velocity in that region of the substrate was indicated by the gentle exponential decline in ChL/ChT as Q_{PD} values increased towards 10. At this energy ratio, ChT/ChG = 1, indicating high grating divisions of uniform chain thickness and gap, with less wobbling or thickness variation due to excessive droplet clustering within each chain, as shown in the inset of Fig. 7b (can also be seen in Fig. S8).

In the energy ratio range $10 < Q_{PD} \leq 100$, the decline in ChL/ChT continues into region D, showing a noticeable levelling from approximately QPI ~ 20 to ~ 100 (at ChL/ChT ~ 10), as depicted in Fig. 7c. A

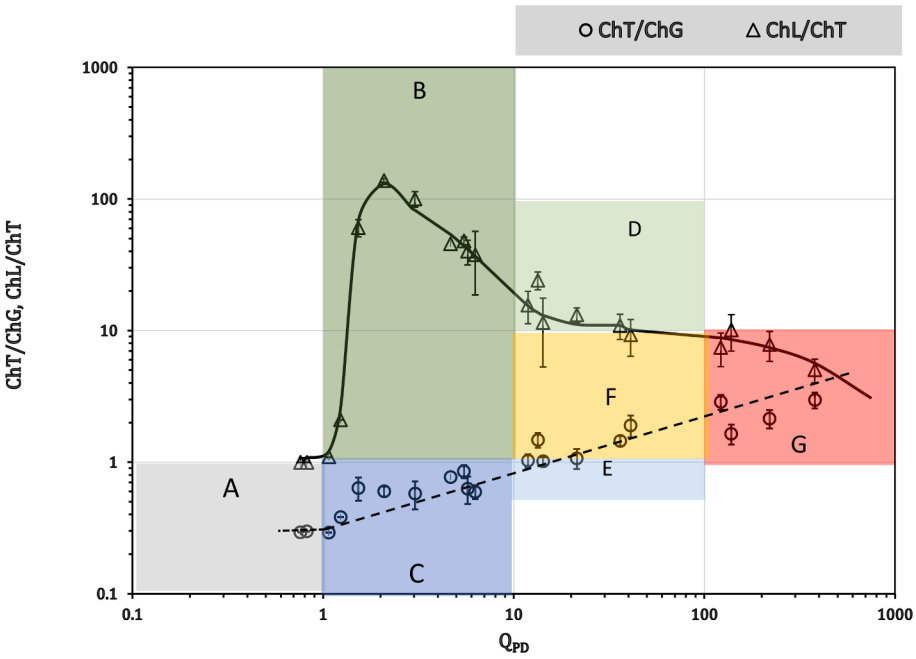

Fig. 6. This is a log–log plot representing the ratio between chain thickness and chain gap (ChT/ChG) and between chain length and chain thickness (ChL/ChT), all against the Q_{PD} ratio for SI configuration. Linear fitting for ChT/ChG is $\log(ChT/ChG) = -0.552 + 0.411\log Q_{PD}$, with $R^2 = 0.9051$.

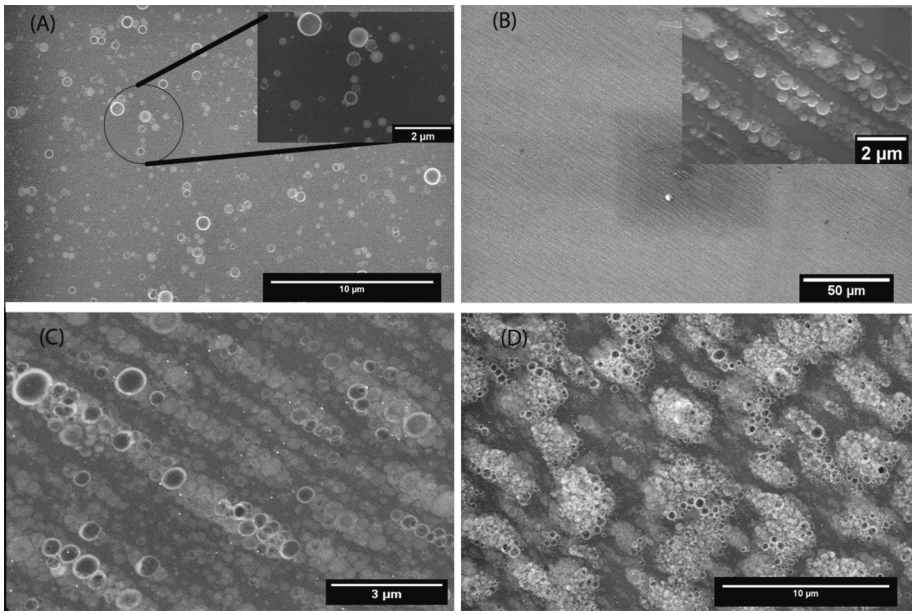

Fig. 7. SEM images of prepared SI configuration sample, with sections related to plots in Fig. 6; (a) shows few and randomly dispersed droplets at a location 6 mm radius from the centre of the substrate, (b) is the structure formation at a location 4 mm radius from the centre of the substrate, (c) at location 2 mm radius from the centre of the substrate, and (d) Image of section at the centre of the substrate. (a) is coherent with section A of Fig. 6, (b) is coherent with data points of ChT/ChG and ChL/ChT within the blue and green regions of C and B, respectively, in Fig. 6. The structure formation in (c) coincides with datapoints ChT/ChG and ChL/ChT within regions D-F and E-F, respectively ($100 \geq Q_{PD} \geq 10$) in Fig. 6, and (d) is equivalent to section G of Fig. 6, where dense columns of droplets dominate the structure pattern.

transition in morphology becomes evident as chain thickness increases relative to chain gap within the range of $0.9 \leq$ ChT/ChG ≤ 2, spanning regions E and F. The interval ($9 \leq$ ChL/ChT ≤ 20) between regions D and F displays a nearly linear distinction. Here, chain length is approximately ten times greater than chain thickness (Fig. 7c). In this region, chain thickness resembles that observed within the range ($6 \leq Q_{PD} \leq 10$). Shortened chain lengths result from increased column formation by superimposed Pickering droplets. The overlay packing of GPFE droplets due to dipole–dipole interactions near the substrate centre responds to the nearly perpendicular magnetic field flux direction towards the substrate surface. This induces columnar repulsion in the y-direction, initiating misalignment, irregularities, and identifiable chain breaks in this region.

For $Q_{PD} > 100$, there is a rapid decrease in ChL/ChT, signifying an increase in chain thickness and a reduction in chain length with more frequent breaks. This indicates the heightened responsiveness of

droplets to external magnetic fields, establishing multiple directional domains among interacting droplets. Consequently, dipole–dipole interactions predominate in the z-direction, while lateral repulsions dominate in the θ direction. This phenomenon primarily arises from the heterogeneous distribution of permanent magnets and their positions beneath the substrate. The formation of thick columns with narrow gaps between them reflects an exponential increase in ChT/ChG, approaching a value of 5, as magnetization energy and viscous effects become 102 times greater than inertia energy. Fig. 7d illustrates this trend observed in region G, highlighting the dominant influence of magnetic field energy, resulting in thicker columns with relatively smaller gaps [11]. This trend persists as ChT/ChG data points increase, while ChL/ChT decreases, converging to the same value at ChT/ChG = ChL/ChT = 4 (where $Q_{PD} \sim 5 \times 10^2$).

The trend data of ChT/ChG were linearly fitted from 1 to 1000 for Q_{PD}. The map's ChL/ChT trend behaviour is like a parabola, which agrees with a previous investigation on the effect of the magnetic field strength on the particle assembly chain length [11]. At $Q_{PD} = 1$ and above, the chain length within the structure reaches its maximum peak before declining due to an increase in magnetic field strength. If a significant portion of the chain length is taken, a short-range existence covered by Q_{PD} between 1 and 10 is observed, with a minimum ChL/ChT ratio of 10.

3.2. Optimisation by magnetic configurations

3.2.1. Compound (CC)

Following the preparation of the GPFE in PVAh using the CC configuration at varying spin speeds, the scanned positions and corresponding energy ratios were correlated with ChT/ChG and ChL/ChT ratios. Standard deviations from their variations were quantified based on high-resolution pattern image processing, as illustrated in Supplementary Fig. S4 and detailed in Table S-VI.

When the data points from Supplementary Table S-VI were mapped onto the constructed Fig. 6, deviations were observed from the predefined ChL/ChT line (indicated by the red arrow in Fig. 8). The extent of deviation was calculated: in region B, ChL/ChT deviated by approximately 30 %, while in region D, the deviation was around 90 %. This analysis underscores that stronger magnetic fields tend to yield longer chains and higher resolutions in chain thickness-to-chain gap ratios [11].

Based on the magnetic profiles examined, it was observed that thin yet elongated chains (up to 0.5 mm) with consistent 10 μm gaps (as depicted in Fig. 8a) are predominantly found in the Q_{PD} range of 0.01 to 0.1. Achieving these elongated chain arrays typically requires magnetic fields of up to 20 mT and radial speeds reaching 1.5 m/s due to centrifugal action. The Q_{PD} range investigated spanned from 1 to 100, with a reference ChL/ChT benchmark of 10.

3.2.2. Concentric (CR)

The setup depicted in Fig. 3d was designed based on the conventional configuration of a flux bridge with opposite poles (N-S). In this configuration, two magnets with opposing poles (North and South) attract each other, establishing directional field lines from the source (North pole) to the sink (South pole). This arrangement enhances the organisation and interaction of magnetised particles along these imaginary flux lines, akin to observations with two permanent magnets. Images were captured using a 50 × magnification objective lens and analysed similarly to previous setups. The experimental process involved applying magnetic fields and varying spin speeds to quantify the energy ratio (Q_{PD}) across the substrate, as detailed in Supplementary Table S-VII.

During the image analysis of the prepared samples, challenges arose in measuring chain lengths due to their extension beyond the frame of the image. Additionally, distinguishing the resolution and array structure was difficult at lower magnifications (20 ×). However, within radial distances of 2 to 6 mm, ChL/ChT values notably exceeded the mapped regions. Long, straight chains with clearly defined chain thickness and gap dimensions were consistently observed over an extended radial range of approximately 10 mm (see Supplementary Fig. S-5(a–f)). This observation was corroborated when plotting ChL/ChT data points against Q_{PD} (Fig. 8b).

An intriguing phenomenon observed was the continuum-trapping effect created by flux lines between the inner and outer magnets of opposite polarity. This mechanism caused the droplets to behave akin to miniature magnets with distinct polarity, fostering linear interactions. Consequently, chain lengths extended significantly beyond the boundaries of the captured image frame within the radial section spanning from 2 mm to 6 mm. As a result, the ChL/ChT ratio was estimated under the assumption that the average chain length in this region approached approximately 1.5 mm.

The data points on the map exhibited a notable deviation of approximately a thousand-fold from the original trend line extending from D to G.

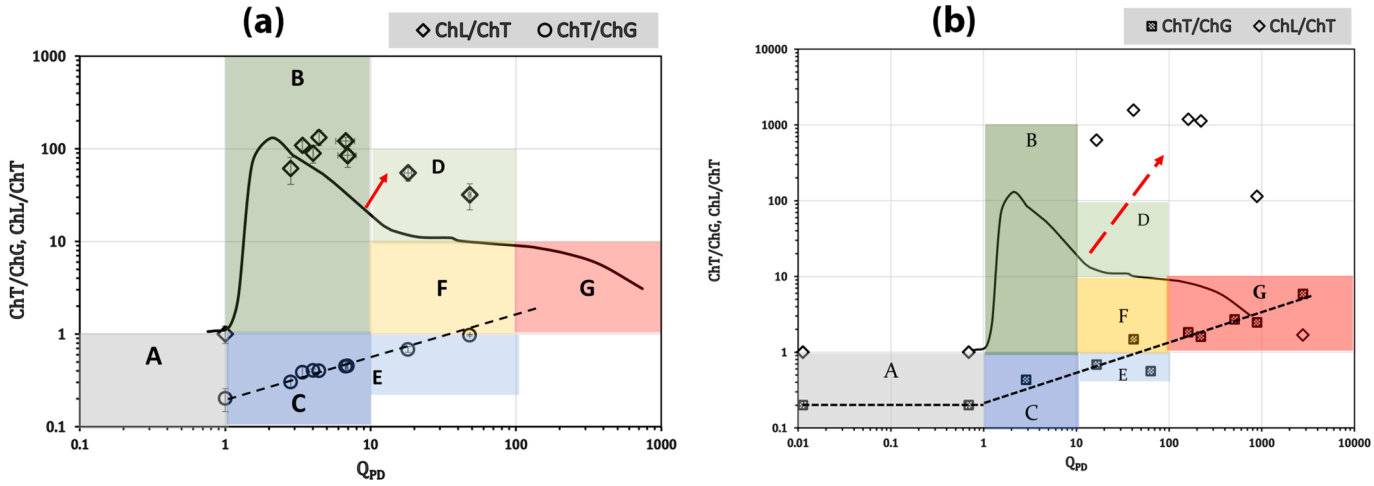

Fig. 8. (a) The calculated sets of data from Table S-VI for magnetic profile CC (b) Map showing data points for CR setup. In (a), the data was quantified from a series of pattern images (example shown in Fig. S-4) and fitted into the pattern profile map. In (b), the data was quantified from a series of pattern images (example shown in Fig. S-5). The ChT/ChG trend approximately followed the original ChT/ChG trend line, further establishing the physical phenomenon of the shear and drag effect on column thickness. The ChL/ChT points between 2 mm and 6 mm are way higher (almost a thousand-fold) than the original ChL/ChT trend line. Linear fitting for CC (ChT/ChG) is $\log(ChT/ChG) = -0.667 + 0.398\log Q_{PD}$, with $R^2 = 0.9828$, while CR (ChT/ChG) is $\log(ChT/ChG) = -0.64 + 0.383\log Q_{PD}$, with $R^2 = 0.904$.

The ChL/ChT trends for both configurations deviated from the SS configuration's constructed ChL/ChT profile. The peak of the longest chain length shifted to higher Q_{PD} values with fairly similar shapes. However, when considering the benchmark of ChL/ChT = 10, the range covered by Q_{PD} under this configuration lies between 1 and 1000.

When looking at the linear fit for ChT/ChG from $Q_{PD} = 1$ to the highest point across all configurations (SS, CC and CR), the intercept point across all configurations averaged 2.5 ± 0.421 (at $Q_{PD} = 1$), the slope across all configurations averaged 0.3973 ± 0.1012. This physically means that with an estimation of a potential energy ratio Q_{PD} at a particular region of interest within a substrate consisting of the magnetic mixture (GPFE), the likelihood of attaining a potential size of ChT relative to ChG is 98.6 %, especially with a standard deviation form the mean slope value as 0.014.

3.3. Defectivity

3.3.1. Single and compound

Expanding nanofabrication into sub-micron scales through self-assembly presents a formidable challenge due to its impact on pattern consistency. This challenge remains a significant barrier to industrial implementation, particularly in accurately assessing the defectiveness of structures produced via specific processes [48]. To tackle this challenge, image analysis proves to be a valuable technique for defect identification and quantification. Defect density can be quantitatively determined as the count or size of defects per unit area within the region of interest [49].

The quantification of defect density involves tracing lines along the chain lengths in binary-processed images at various locations across the substrate. As previously discussed, the profile scan data provides insights into the distribution of droplets and gaps within the scanned region. Droplets appear as white pixels with values greater than zero, while gaps appear as black with values equal to zero. Supplementary Fig. S6(a and b) illustrates binary-processed images corresponding to Q_{PD} values of 17.5 for (a) and 2.28 for (b). Their respective insets depict 3-dimensional plots showcasing specific scan lines, scan line lengths (μm), and binary pixel intensities. The resolution of these binary points is 168 nm/pixel. By analysing the plot profiles, we quantified the length covered by gaps by counting zero-intensity binary points and multiplying by the resolution, using the methodology detailed in Supplementary S.2.1. The defect length was calculated by dividing the total gap length by the scan line length. Given multiple scan lines, average values and their standard deviations were computed. Analysis of Supplementary Fig. S6 data revealed defect densities of 4.3 % with a standard deviation of 0.019 and 11.6 % with a standard deviation of 0.029. This outcome aligns with expectations, as systems with higher magnetic energy exhibit denser packing with reduced interstitial spaces compared to systems where inertial energy predominates over magnetic forces.

It is crucial to consider the chain lengths obtained from various energy ratio values when assessing defectivity. Within an array featuring chain breaks, each gap represents a defect that must be quantified. These gaps denoted as ChM were measured and added to the defects found within the chains. The calculated values reflecting the final estimate of defectivity, accounting for chain lengths, are presented in Supplementary Table S-VIII.

The summary of results indicates that higher values of the ratio Q_{PD} lead to increased defectivity and structural instability. However, the overall defectivity does not exhibit a significant difference across the three energy ratios. On average, it amounts to 21.2 % for CC and 23 % for SI.

3.3.2. Concentric

A study was conducted to assess the consistency of chain lengths in a high-resolution ChT/ChG section of a sample compared to other magnetic system configurations. Pixel values were obtained by drawing profile lines across each line of the binary image. Pixels with values greater than zero were tallied, while those equal to zero were counted separately (refer to Supplementary Fig. S7). Defectivity was calculated as the total gap size (number of zero pixels × 0.168 μm/pixel) divided by the overall scan length. The results from the selected profile scans are summarised in Supplementary Table S-IX.

The final defectivity averaged approximately 14.1 %, compared to 21 % for CC configurations. The concentric setup appears to be a superior technique for achieving enhanced structural resolution compared to single or compound magnet setups.

The occurrence of fewer defects would likely result if there were no minor deviations in the chain alignment along adjacent imaginary flux lines. These deviations occur at dipole points where one droplet is significantly larger than others, leading smaller droplets to separate from it due to mutual repulsion, thus creating noticeable gaps that appear discontinuous in plot profiles. Microscope images taken in reflection mode illustrate more visible droplets above the profile and fewer below. The limitations in capturing chain continuity are evident in the SEM image (Fig. 9) of a sample prepared using the CC setup at 3000 rpm spin speeds. A yellow straight line in the image represents an example of a scan profile used to measure defectivity. While the chain remains continuous, deviations from its straight path are observed (marked by red oval circle 2), and another gap is detected due to branching (marked by red oval 3). The impact of branching is more apparent in yellow oval 1, where larger droplets with multiple polarities on their surface attract multiple droplets, leading to branching at specific points.

In general, when using self-assembly techniques, defectivity is unavoidable, and this also applies to nanofabrication methods. However, defectivity can be reduced or managed to some extent, which makes the manufactured template useful in applications that do not rely entirely on structural precision. In the method of fabrication carried out in this work, the opposite pole concentric magnetic setup proved to be more precise than other formations and is therefore recommended for future use. The precision can be further improved by using monodispersed Pickering emulsion droplets to reduce chain branching and bending within thin films.

4. Conclusion

This work presents a modified approach on the magnetic and spin-coating self-assembly of nanoparticles. The magnetic configuration and spin speed manipulation on the gold-pickering ferrofluid emulsion

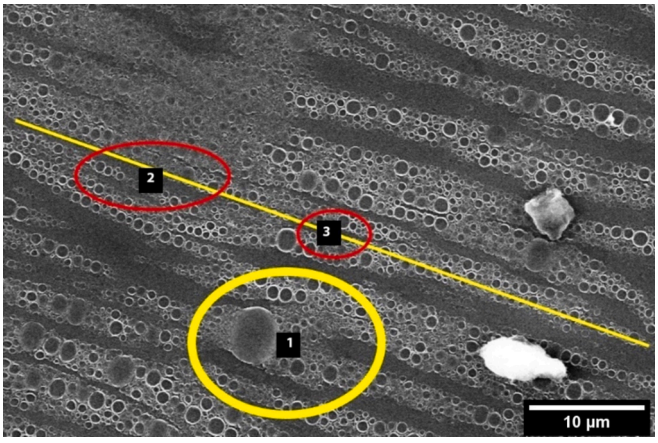

Fig. 9. An SEM image of chain interactions upon a silicon wafer. The yellow oval 1 shows evidence of big droplet initiating branching of chains, The yellow straight line 2 is an example of profile line scan for detecting defection which the highlights its deviation due to shifting of chain from straight path in the form of red oval 2 and 3. (For interpretation of the references to colour in this figure legend, the reader is referred to the web version of this article.)

in aqueous polyvinyl alcohol revealed various degrees of chain morphology output. An increased spin speed greater than 700 rpm was necessary for evaporating water and drying the polymer to trap the organised GPFE structure. The contention between magnetic packing energy and fluid inertia energy dictates the type of chain morphology in terms of chain thickness, length, and gaps. When the magnetic packing energy was 100 times greater than the fluid flow energy, the chain thickness became greater than the chain gap. When the packing energy to fluid flow energy ratio becomes unity and below, the GPFE droplets are randomly dispersed. CR configuration gave a better chain morphology profile with longer chain lengths and a steady graduating grating order among all configurations. This revealed the essence and effect of the flux bridge between two opposite magnetic poles as a channel for interlinking GPFE droplets with an average defectivity of 14 % (~33 % decrease from both single and compound configurations). Beyond these optimization preferences is the realization of a new relationship where the ratio between magnetic energy and fluid inertia energy (by spin coating) determines the ratio between magnetized chain thickness and gaps in between them with a 98.6 % likelihood of estimation. This method of submicron fabrication and its output can play a role in utilising the variance in grating order for diffracting far-infrared/microwave electromagnetic waves to enhance the optical performance of the device. Like most product outputs using self-assembly techniques, products from SDSA are probably not intended for applications that require a high degree of accuracy because of their degree of defectivity.

CRediT authorship contribution statement

Paul Okpozo: Writing – review & editing, Writing – original draft, Visualization, Validation, Investigation, Formal analysis, Data curation, Conceptualization. **James Njuguna:** Writing – review & editing, Visualization, Supervision, Project administration, Funding acquisition. **Sheikh Islam:** Validation, Supervision, Resources. **Kindness Uyanga:** Writing – review & editing, Visualization, Validation, Methodology, Formal analysis. **Ketan Pancholi:** Writing – review & editing, Writing – original draft, Supervision, Project administration, Investigation, Formal analysis, Conceptualization.

Declaration of competing interest

The authors declare that they have no known competing financial interests or personal relationships that could have appeared to influence the work reported in this paper.

Data availability

Data will be made available on request.

Acknowledgements

We thank Alan McClean, David Howie, and Patrick Kane of the School of Engineering (RGU) for technical laboratory assistance. Lastly, we wish to thank the School of Pharmacy and Life Sciences (RGU) for granting access to their facilities, particularly Emily Hunter, for her assistance with scanning electron microscopy.

Author statement

I am an author on this submission, have adhered to all editorial policies for submission as described in the Information for Authors, attest to having met all authorship criteria, and disclosed all potential conflicts of interest for inclusion on the title page of the submission

.

Appendix A. Supplementary data

Supplementary data to this article can be found online at https://doi.org/10.1016/j.jmmm.2024.172577.

References

[1] R. Dreyfus, D. Lacoste, Bibette, J. Baudry, Measuring colloidal forces with the magnetic chaining technique, Eur. Phys J. E 28 (2009) 113–123, https://doi.org/10.1140/epje/i2008-10414-4.
[2] W. Libaers, B. Kolaric, R. Vallee, J. Wong, J. Wouters, V. Valev, T. Verbiest, K. Clays, Engineering Colloidal Photonic Crystals with Magnetic Functionalities, Colloids Surf A Physicochem Eng Asp 339 (1–3) (2009) 13–19, https://doi.org/10.1016/j.colsurfa.2009.01.012.
[3] L. He, M. Wang, J. Ge, Y. Yin, Magnetic assembly route to colloidal responsive photonic nanostructures, Acc. Chem. Res. 45 (9) (2012) 1431–1440. HTTPS://DOI.ORG/10.1021/AR200276T.
[4] M. Ohring, Magnetic Properties of Materials. In: Engineering Materials Science. s.l, Elsevier, 1995, pp. 711–746.
[5] A. Gupta, R.T. Pardasani, P. Pardasani, Magnetic properties of Paramagnetic Compounds, 1st edition, Springer, Berlin, 2017.
[6] J. Xu, M. Shang, X. Ni, Y. Cao, Strategy based on rapid self-assembly of magnetic nanoparticles for construction of photonic crystals, ACS Applied Nano Materials 3 (8) (2020) 8052–8059, https://doi.org/10.1021/acsanm.0c01481.
[7] J. Ge, Y. Hu, Y. Yin, Highly tunable superparamagnetic colloidal photonic crystals, Angew. Chem. Int. Ed. 46 (39) (2007) 7428–7431, https://doi.org/10.1002/ange.200701992.
[8] Y. Dubi, Y. Sivan, "Hot" electrons in metallic nanostructures—non-thermal carriers or heating? Light Sci. Appl. 8 (1) (2019) 1–8, https://doi.org/10.1038/s41377-019-0199-x.
[9] R.J. Powell, Photoconductive processes in Al2O3 films, J. Appl. Phys. 47 (10) (1976) 4598–4604, https://doi.org/10.1063/1.322385.
[10] X. Zhu, Surface photochemistry, Annu. Rev. Phys. Chem. 45 (1) (1994) 113–144, https://doi.org/10.1016/0039-6028(94)90712-9.
[11] Z. Zhu, S. Wu, C. Zhang, J. Zhou, Length Measurement of Chain-Like Structure Of Micron Magnetic Particles Dispersing In Carrier Fluid affected by Magnetic Field, J Supercond. Nov Magn 34 (2021) 805–816, https://doi.org/10.1007/s10948-020-05779-6.
[12] U. Soni, R.P. Desai, Analysing Magnetic Nanofluid Structure, 012009(1–8), Phys. Fluids 34 (2022), https://doi.org/10.1063/5.0077322.
[13] T. Mou, G.A. Flores, J. Liu, J. Bibette, J. Richard, The Evolution of Field Induced Structure Of Confined Ferrofluid Emulsion, Int. J. Mod Phys B 8 (20) (1994) 2779–2787, https://doi.org/10.1142/S0217979294001123.
[14] E.M. Lawrence, M.L. Ivey, G.A. Flores, J. Liu, J. Bibette, J. Richard, Field-Induced Structure of Confined Ferrofluid Emulsion, Int. J. Mod Phys B 8 (20) (1994) 2765–2777, https://doi.org/10.1142/s0217979294001111.
[15] U. Hartmann, H.H. Mende, Experimental Investigation of Néel Relaxation Effects On Magnetostatic Properties Of A Ferrofluid, J. Magn & Magnet Mat 45 (2–3) (1984) 409–414, https://doi.org/10.1016/0304-8853(84)90038-6.
[16] J. Landers, S. Salamon, H. Remmer, F. Ludwig, H. Wende, Simultaneous Study of Brownian and Neel Relaxation Phenomena In Ferrofluids By Mossbauer Spectroscopy, Nano Lett. 16 (2) (2016) 1150–1155, https://doi.org/10.1021/acs.nanolett.5b04409.
[17] B.P. Binks, J.H. Clint, Solid Wettability From Surface Energy Components: Relevance To Pickering Emulsions, Langmuir 18 (2002) 1270–1273, https://doi.org/10.1021/la011420k.
[18] S.M. Guttula, Self-Assembly Of Colloidal Latices at Pickering Emulsion Interface, Texas, Thesis In Applied Physics, Texas Tech University, 2007.
[19] K. Larson-Smith, D.C. Pozzo, Scalable Synthesis Of Self-Assembling Nanoparticle Clusters Based On Controlled Steric Interactions, Soft Matter 7 (2011) 5339–5347, https://doi.org/10.1039/C0SM01497D.
[20] K. Larson-Smith, D.C. Pozzo, Pickering Emulsion Stabilized By Nanoparticle Surfactants, Lagmuir 28 (32) (2012) 11725–11732, https://doi.org/10.1021/la301896c.
[21] R. Aslam, W. Gonzalez-Vinas, Pattern formation in spin-coating of hybrid colloids in different magnetic field configurations, J. Phys. D Appl. Phys. 52 (2019) 344001, https://doi.org/10.1088/1361-6463/ab2795.
[22] R. Aslam, K. Shahrivar, J. De Vicente, W. Gonzalez-Vinas. Magnetorheology Of Hybrid Colloids Obtained By Spin Coating And Classical Rheometry. Smart Materials And Structures 2016, 25(7), P. 075036, DOI: 10.1088/0964-1726/25/7/075036.
[23] M. Pichumani, W. Gonzalez-Vinas, Spin -Coating of Dilute Magnetic Colloids In A Magnetic Field, Magnetohydrodynamics 47 (2) (2011) 191–199.
[24] M. Pichumani, W. Gonzalez-Vinas, Magnetorheology From Surface Coverage Of Spin-Coated Colloidal Films, Soft Matter 9 (2013) 2506–2511, https://doi.org/10.1039/C2SM27682H.
[25] P. Okpozo, K. Pancholi, Study of Spatial Organisation of Magnetic Field Directed Gold-Pickering-Ferrofluid-Nanoemulsion in Spin Coated Film. *Hybrid*, Advances 100018 (2023), https://doi.org/10.1016/j.hybadv.2023.100018.
[26] N.T. Nguyen, Micro-Magnetofluidics. Interactions Between Magnetism And Fluid Flow On The Microscale, Microfluid Nanofluid (2012).
[27] P. Okpozo, Y. Dwivedi, D. Huo, K. Pancholi, Enhancement of infrared absorption through a patterned thin film of magnetic field and spin-coating directed self-

assembly of gold nanoparticle stabilised ferrofluid emulsion, RSC Adv. 13 (2023) 23955–23966, https://doi.org/10.1039/D3RA01369C.
[28] O.P. Okpozo, Magnetic Field Directed Self-Assembly Of Gold Pickering Emulsion For Preparing Patterned Film. Robert Gordon University, Phd Thesis. Openair 2022 [Online]: https://doi.org/10.48526/rgu-wt-1987909.
[29] Pi-Kem, Electronics and Photonics Research Catalogue, [online]. (2019), available at: https://www.pi-kem.co.uk/images/cms/Electronics%20&%20Photonics%20Research%20-%20For%20web.pdf [Accessed 17 Novembr 2021].
[30] R. Gupta, P. Gupta, C. Footer, B.G. Stenning, J. Darr, K. Pancholi, Tuneable Magnetic Nanocomposites For Remote Self-Healing, Sci Rep 12 (2022) 10180. Https://Doi.Org/10.1038/S41598-022-14135-8.
[31] M. Mohsen-Nia, H. Modarress, Viscometric Study Of Aqueous Poly(Vinyl Alcohol) Pva Solutions As A Binder In Adhesive Formulations, J. Adhesion Sci. Technol. 20 (12) (2012) 1273–1280, https://doi.org/10.1163/156856106778456636.
[32] Fermigier M. and Gast A. P. Structure evolution in a paramagnetic latex suspension, Journal of Colloid and Interface Science, 1992, Vol. 154, Iss. 2, pp. 522-539, https://doi.org/10.1016/0021-9797(92)90165-I.
[33] J. Nowak, D. Borin, S. Haefner, A. Richter, S. Odenbach, Magnetoviscous effect in ferrofluids diluted with sheep blood, J. Magn. Magn. Mater. 442 (2017) 383–390, https://doi.org/10.1016/j.jmmm.2017.07.029.
[34] J. Danglad-Flores, S. Eickelmann, H. Reigler, Evaporation behaviour of a thinning liquid film in a spin coating setup: Comparison between calculation and experiment, Engineering Reports, Wiley 9 (3) (2021) 12390, https://doi.org/10.22541/au.161462306.64671452/v1.
[35] M.M. Ali, K.S. Lim, H.S. Yang, W.Y. Chong, W.S. Lim, H. Ahmad, Direct period measurement for fine Bragg grating using an optical imaging technique, Appl. Opt. 52 (22) (2013) 5393–5397, https://doi.org/10.1364/AO.52.005393.
[36] J. Deng, J. Dong, P. Cohen, Rapid Fabrication and Characterisation of SERS Substrates, Procedia Manuf. 26 (2018) 580–586, https://doi.org/10.1016/j.promfg.2018.07.068.
[37] T. Maß, V. Nguyen, U. Schnakenberg, T. Taubner, Tailoring Grating Strip Widths for Optimising Infrared Absorption Signals of An Adsorbed Molecular Monolayer, Opt. Express 27 (8) (2019) 10524–10532, https://doi.org/10.1364/OE.27.010524.
[38] T. Wang, V.H. Nguyen, A. Buchenauer, U. Schnakenberg, T. Taubner, Surface Enhanced Infrared Spectroscopy with Gold Strip Gratings, Opt. Express 21 (7) (2013) 9005–9010, https://doi.org/10.1364/OE.21.009005.
[39] W. Mingsheng, H. Le, Y. Yadong, Magnetic field guided colloidal assembly, Mater. Today Elsevier (2013) 110–116, https://doi.org/10.1016/j.mattod.2013.04.008.
[40] T. Kang, M. Hulsen, J. Den Toonder, Dynamics Of Magnetic Chains In A Shear Flow Under The Influence Of A Uniform Magnetic Field, Phys. Fluids 24 (4) (2004) 2001–2018, https://doi.org/10.1063/1.4704822.
[41] M.O. Maria, Study Of Static Magnetic Properties of Transformer Oil Based Magnetic Fluids For Various Technical Applications Using Demagnetizing Field Correction, J. Nanomater. (2017), https://doi.org/10.1155/2017/5407679.
[42] A. Emslie, F. Bonner, L. Peck, Flow of a Viscous Liquid on a Rotating Disk, J. Appl. Phys. 29 (1958) 858–862, https://doi.org/10.1063/1.1723300.
[43] C.J. Lawrence, W. Zhou, Spin Coating Of Non-Newtonian Fluids, J. Nonnewton. Fluid Mech. 39 (1991) 137–187, https://doi.org/10.1016/0377-0257(91)80010-H.
[44] D.E. Weidner, Analysis of the Flow of a Thin Liquid Film on the Surface of a Rotating, Curved, Axisymmetric Substrate, Phys. Fluids 30 (2018) P. 082110, https://doi.org/10.1063/1.5034359.
[45] P. De Gennes, P. Pincus, Pair Correlations in Ferromagnetic Colloid, Kondensierten Materie 11 (1970) 189–198, https://doi.org/10.1007/BF02422637.
[46] R. Ganguly, I.K. Puri, Microfluidic Transport In Magnetic Mems And Biomems, Wiley Interdiscip. Rev. Nanomed Nanobiotechnol 2 (4) (2010) 382–399, https://doi.org/10.1002/wnan.92.
[47] P. Williams, F. Carpino, M. Zborowski, Characterisation Of Magnetic Nanoparticles Using A Programmed Quadrople Magnetic Field-Flow Fractionating, Philosophica Transactions Royal Society of America 368 (2010) 4419–4437, https://doi.org/10.1098/rsta.2010.0133.
[48] G. Whitesides, J. Kriebel, B. Mayers, Self-Assembly And Nanostructured Materials, in: Nanoscale Assembly, Springer, Boston, Ma, 2005, pp. 217–239.
[49] Simão C, Tuchapsky D, Khunsin W, Amann A, Morris M A and Torres C S. Defect analysis and alignment quantification of line arrays prepared by directed self-assembly of a block copolymer. In Metrology, Inspection, and Process Control for Microlithography XXVIII (Vol. 9050, pp. 594-603) 2014. SPIE, https://doi.org/10.1117/12.2046075.

SUPPLEMENTARY INFORMATION

Fabrication with Magnetic-Spin Coating: Influence of Magnetic-Inertia Energy Ratio on Gold-Pickering Ferrofluid Droplet Assembly Morphology

Paul Okpozo[1], James Njuguna[1,2], Sheikh Islam[1], Kindness Uyanga[3], Ketan Pancholi[1]

[1]School of Engineering, Sir Ian Wood Building, Robert Gordon University, Garthdee, Aberdeen, AB10 7GJ, UK

[2]National Subsea Centre, 3 International Ave., Dyce, Aberdeen, AB21 0BH, UK

[3]Department of Mechanical Engineering, City University of Hong Kong, 83 Tat Chee Avenue, Kowloon, Hong Kong

Corresponding Authors: p.okpozo@rgu.ac.uk; k.pancholi2@rgu.ac.uk

S. 1.1) Magnetic Hysteresis of Oleic coated magnetite and derived Magnetic property

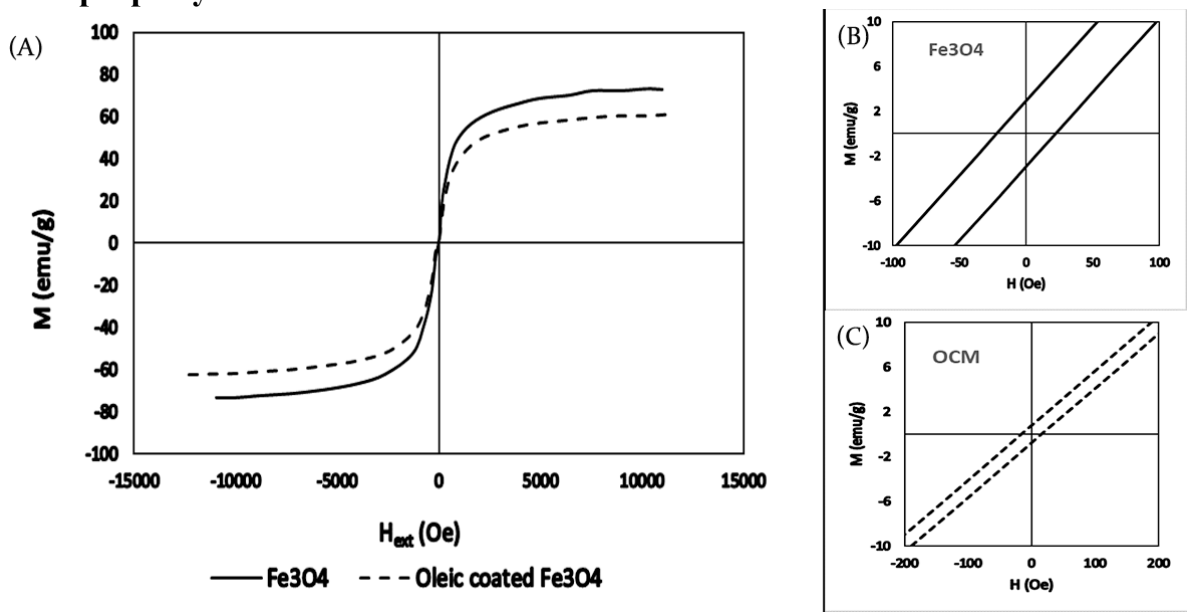

Figure S-1: (A) Magnetic hysteresis for magnetite and Oleic coated magnetite (OCM), (b) and (c) presents a magnified range of the hysteresis curve to obtain coercivity (H_o) for both magnetite and OCM materials respectively.

S. 1.2) Size Distribution ferrofluid emulsion

The size distribution of ferrofluid droplet after ultrasonication was determined using the Malvern Nano Zeta sizer equipment. The size distribution is bimodal in representation in Figure S-2.

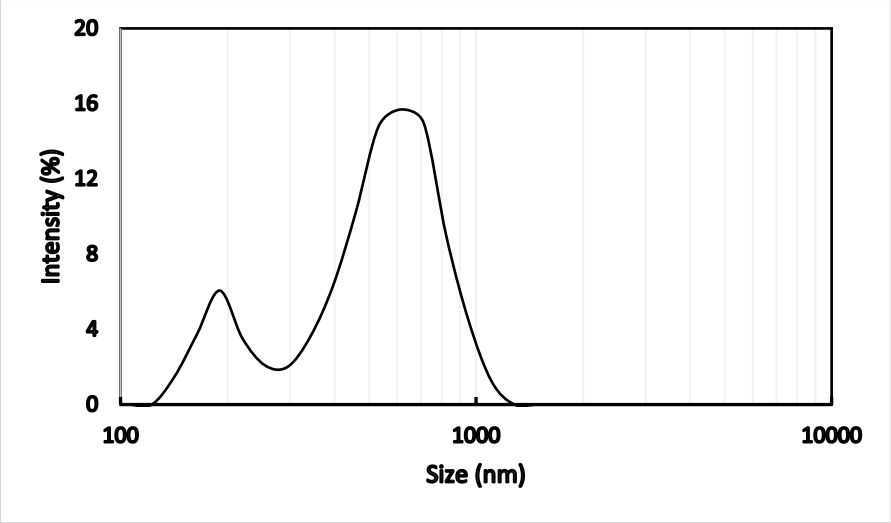

Figure S-2: Size distribution of ultrasonicated gold pickering ferrofluid droplets in DI water (Reproduced from ref. 28 with permission from RGU repository).

Droplet distribution was then managed by centrifugal action to separate bigger droplets from smaller droplets, therefore reducing the broad range of size distribution. Table S-1 shows one example of how a 200 nm size distribution was achieved using an angular (rotation) speed of 4500 rpm.

Table S-1: Size distribution data of ferrofluid in water emulsion following different 4500 rpm spin speed and spin time (Reproduced from ref. 28 with permission from RGU repository).

Speed (RPM)	Time (min)	mean1 (nm)	mean2 (nm)	fraction1	fraction2	StD1 (nm)	StD2 (nm)
4500	0	609.7	170.4	0.804	0.196	240	15.5
4500	5	562.5	218.7	0.079	0.921	150.6	36.18
4500	10	220		1		75.7	
4500	15	208.1		1		50.27	
4500	20	207		1		28.62	

Std1 & StD2 are standard deviations, mean1 & mean2 are means, and fractions 1 & 2 are fractions of the bimodal peaks.

As time increased during the centrifugal process, the bigger droplets moved to the bottom of the tube, with the smaller droplets least mobilised. This is especially true because the ferrofluid is approximately 1.6g/ml (denser than the dispersing liquid—water).

S. 1.3) Liquid height (h_o) on a substrate

1ml of aqueous PVA was deposited on glass substrate and allowed to spread under its own weight before taking contrast images via transmisson mode to observe the liquid height from the surface of the flat substrate. This investigation aimed to estimate the length of dipole chains to be formed within the liquid thickness. Figure S-1 presents images and final fitted plot for all concentrations (or density) of tested PVA solutions.

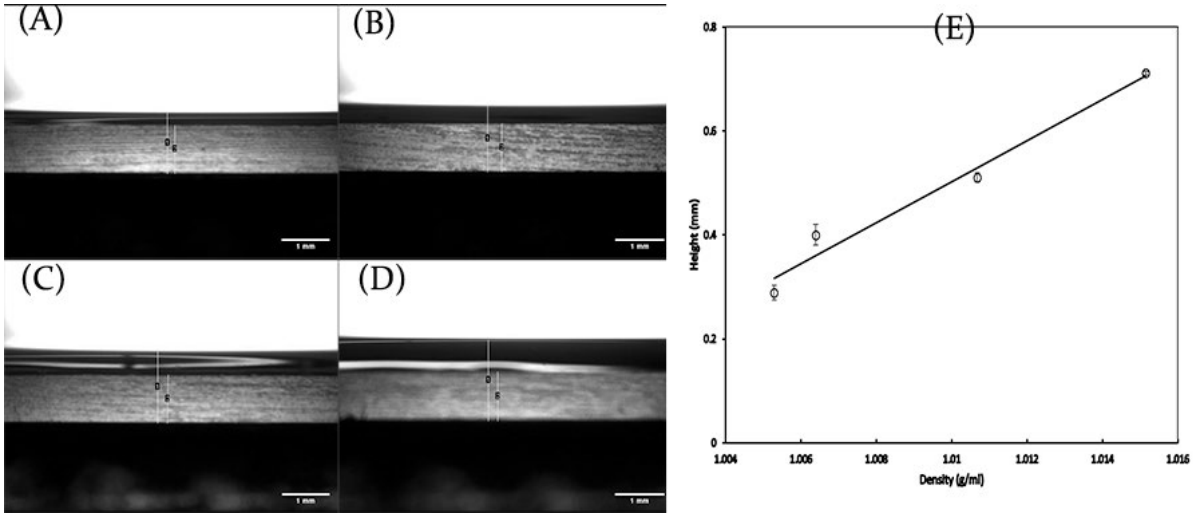

Figure S-3: Aqueous PVA on substrate with densities with scale bar of 1mm (a) 1.00529 g/ml, (b) 1.0064 g/ml, (c) 1.01068 g/ml, (d) 1.015145 g/ml, and (d) is the representative fitted plot of height vs density of polymer with fit as $39.48\rho - 39.37251$*, having an R squared of 0.9721.*

S.2) Image Processing Technique

S. 2.1) Simple Code for Chain thickness and gap Profile scan

```
Sub CL-CT_Scan()
Dim i, M, rw, CntCh, CntGap, K, L, CL1, CL2, d, W As Integer
'This is for estimating the chain thickness and gap from image scan
‘i is counter for number of column/lines to be scanned, M = Number
of ‘scanned ‘lines, CntCH = Chain thickness pixel counts, CntGap =
Chain ‘gap pixel ‘counts, K, CL2 = variable associated with CntCH,
L, CL1 = ‘variable ‘associated with CntGap, d = pixel count (rows -
W).
M = Sheet3.Cells(30, 25).Value     'number of columns to be scanned
For i = 1 To M
CntCh = 0
CntGap = 0
K = 1
L = 1
W = Sheet3.Cells(30, i * 2 + 24).Value   'number of rows per column
For d = 2 To W Step 1
If Sheet3.Cells(d, 2 * i).Value > 0 Then
If CntCh = 0 Then
K = K + 1
CL2 = K
Else
K = CL2
End If
CntCh = CntCh + 1
Sheet3.Cells(K + 31, i * 2 + 24) = CntCh
CntGap = 0
Else
If CntGap = 0 Then
L = L + 1
CL1 = L
Else
```

```
L = CL1
End If
CntGap = CntGap + 1
Sheet3.Cells(L + 31, i * 2 + 25) = CntGap
CntCh = 0
End If
Next d
Next i
End Sub
```

S. 2.2) Single Magnetic Setup

Table S-II: Example of scan plot profile for one of the red lines from Figure 5(b) with X as pixel divisions (168nm/pixel) and Y as the binary pixel intensity.

Red Line (B)		Red Line (D)		Red Line (F)		Red Line (H)	
X (divisions-nm/pixel)	Y (pixel intensity)	X (divisions-nm/pixel)	Y (pixel intensity)	X (divisions-nm/pixel)	Y (pixel intensity)	X (divisions-nm/pixel)	Y (pixel intensity)
0	255	0	0	0	255	0	255
168	255	168	0	168	238	168	255
337	0	337	0	337	247	337	0
505	0	505	0	505	255	505	0
673	0	673	0	673	255	673	0

Table S-III: Example of output from simple program (S.2.1) that counted number of pixels in each chain block to identify chain thickness and chain gaps within the scanned profile. CntCL and CntGap is number of pixel counts for a chain and gap respectively.

Scan profile B		Scan Profile D		Scan Profile F		Scan Profile H	
Total No. Rows 997		Total No. Rows 965		Total No. Rows 971		Total No. Rows 933	
CntCL	CntGap	CntCL	CntGap	CntCL	CntGap	CntCL	CntGap
2	4	5	34	5	17	2	68
2	21	5	2	7	34	3	2
2	8	2	2	5	17	3	3
6	8	2	10	2	3	10	7

Table S-IV: Summary of results obtained from image analysis of sample prepared under 3500 rpm spin speed.

3500 RPM									
r (m)	**CG (µm)**	**CT (µm)**	**CL (µm)**	**SD-CG**	**SD-CT**	**SD-CL**	**CL/CT**	**CT/CG**	**Qpi**
0.001	2.32	2.66	42.7	0.14	0.23	5.32	16.05	1.15	13
0.0025	2.65	2.46	93	0.22	0.2	1.72	37.8	0.93	5
0.0042	2.82	2.15	209	0.5	0.07	19.0	97.2	0.73	2
0.0049	3.05	1.94	98	0.58	0.14	13.5	50.5	0.64	1.5
0.0057	5.03	1.215	1.21	0.32	0.076	0.34	1.0	0.24	1

SD represents Standard deviation

Table S-V: Summary of pattern morphology image analysis for PVA 15.2mPas for SS setup

2000	RPM								
R (m)	CG (µm)	CT (µm)	CL (µm)	SD-CG	SD-CT	SD-CL	CL/CT	CT/CG	Qpi
0.0001	7.26E-01	3.59E+00	11.6	0.113	0.445	2.34	7.26E+03	4.95E+00	741.6753
0.0006	1.17E+00	3.35E+00	2.50E+01	0.197634	0.331624	8.39374	1.95E+03	2.87E+00	121.9136
0.0028	1.77E+00	1.89E+00	2.49E+01	0.281709	0.120368	4.298348	6.32E+02	1.07E+00	21.41232
0.0055	2.85E+00	1.70E+00	6.41E+01	0.721376	0.134699	5.718723	5.19E+02	5.96E-01	6.282408
0.0061	3.41E+00	1.40E+00	5.82E+00	0.532055	0.887868	1.382119	5.59E+02	4.12E-01	4.787218
0.0096	4.08E+00	1.215	1.21	0.742	0.0142	0.113	4.25E+02	2.98E-01	0.821803
2500	RPM								
R (m)	CG (µm)	CT (µm)	CL (µm)	SD-CG	SD-CT	SD-CL	CL/CT	CT/CG	Qpi
0.0001	1.02E+00	3.04E+00	15.3	0.125	0.743	1.84	1.02E+04	2.97E+00	379.7368
0.0009	1.45E+00	2.75E+00	2.55E+01	0.240141	0.134112	2.36005	1.61E+03	1.90E+00	41.03946
0.0023	2.36E+00	2.41E+00	2.76E+01	0.397652	0.190433	3.732972	1.03E+03	1.02E+00	14.24194
0.0042	2.74E+00	1.72E+00	6.90E+01	0.455631	0.09421	3.03916	6.53E+02	6.28E-01	5.728691
0.0057	3.34E+00	1.51E+00	1.54E+01	0.772788	0.052178	4.219714	5.85E+02	4.53E-01	2.939852
0.0085	4.14E+00	1.215	1.21	0.025	0.321	0.254	4.87E+02	2.94E-01	0.760879
3000	RPM								
R (m)	CG (µm)	CT (µm)	CL (µm)	SD-CG	SD-CT	SD-CL	CL/CT	CT/CG	Qpi
0.0001	1.31E+00	2.82E+00	22.1	0.035	0.176	1.2	1.31E+04	2.14E+00	219.7548

0.0006	1.91E+00	2.77E+00	3.03E+01	0.700762	0.362586	0.700762	3.18E+03	1.45E+00	36.12242
0.0017	2.56E+00	2.62E+00	4.09E+01	0.446337	0.07389	0.446337	1.50E+03	1.03E+00	11.87122
0.0031	2.66E+00	2.27E+00	8.66E+01	0.64685	0.147469	0.64685	8.59E+02	8.51E-01	5.480763
0.0044	3.02E+00	1.68E+00	1.24E+02	0.538161	0.210776	0.538161	6.85E+02	5.56E-01	3.033705
0.0064	4.63E+00	1.215	1.21	0.453	0.075	0.325	7.23E+02	2.63E-01	1.235146
3500	RPM								
R (m)	CG (µm)	CT (µm)	CL (µm)	SD-CG	SD-CT	SD-CL	CL/CT	CT/CG	Qpi
0.0001	1.70E+00	2.80E+00	28.3	0.351	0.183	0.642	1.70E+04	1.65E+00	138.3877
0.001	2.32E+00	2.66E+00	4.27E+01	1.40E-01	2.30E-01	5.32E+00	2.32E+03	1.15E+00	13.38585
0.0025	2.65E+00	2.46E+00	9.30E+01	0.217497	0.18849	1.721369	1.06E+03	9.29E-01	4.659019
0.0042	2.82E+00	2.15E+00	2.09E+02	0.522639	0.073206	19.06515	6.72E+02	7.63E-01	2.087711
0.0049	3.05E+00	1.94E+00	9.83E+01	0.577078	0.139186	13.47646	6.22E+02	6.36E-01	1.531205
0.0057	5.03E+00	1.215	1.21	0.321	0.076	0.342	8.83E+02	2.41E-01	1.071372

S. 2.3) Compound Magnetic Setup

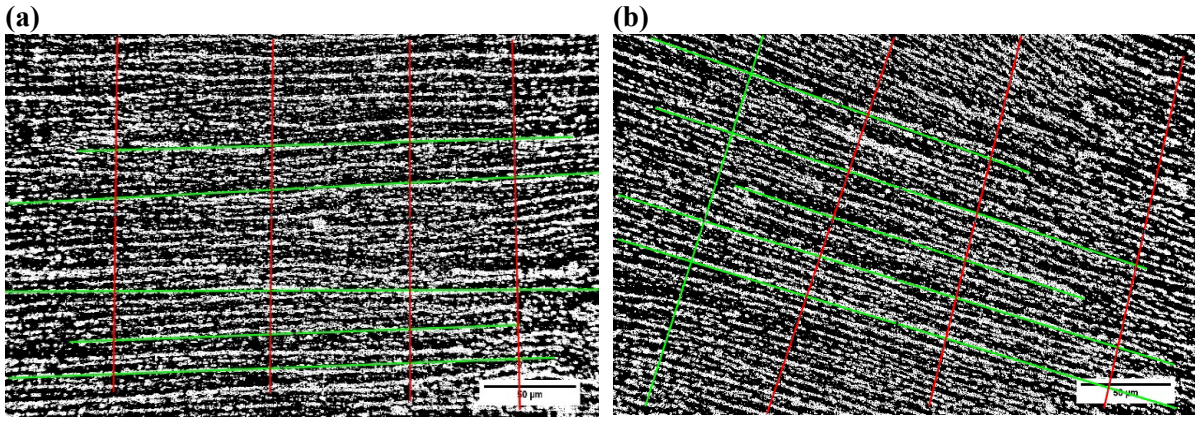

Figure S-4: Binary processed image profile of (a) CCC at radius 8.2mm under speed 2000rpm (b) CCC at radius 4.4mm from centre under speed 3500 rpm. Scalebar is 50um.

Table S-VI: Some data of the test magnetic setups, CCC and CRC showing ratios QPI against CL/CT and CT/CG with their respective standard deviation values (SD)

Magnet Profile	**r (mm)**	**Speed (rpm)**	**Q_{PI}**	**CL/CT**	**SD**	**CT/CG**	**SD**
CCC	14.1	2500	1.0	1.0	0.211	0.20	0.044
	8.1	2000	4.02	89.76	19.56	0.406	0.056
	7.7	2500	3.40	108.78	12.94	0.385	0.013
	7.4	3000	2.82	61.10	19.87	0.304	0.055
	7.2	2500	6.95	84.8	22.00	0.454	0.045
CRC	7	2000	18.1	54.8	9.824	0.682	0.049
	6.6	3500	4.41	132.92	24.70	0.401	0.045
	6.5	3500	6.75	121	12.22	0.451	0.053
	6.5	3500	6.75	121	12.22	0.451	0.053
	5.3	3000	48.1	31.9	9.98	0.972	0.017

S. 2.4) Concentric Magnetic Setup

Table S-VII: Energy ratio (QPI) determined from magnetic profile shown in Fig. 3c and emulsion property from Table I and preparation angular speed 3500 rpm

r(mm)	B (mT)	Q_{PI}
0.1	55	2.78E+03
1	44	889.2264
2	31	220.699
4	19	41.45283
6	14.7	16.54209
8	53	161.2756
10	105.4	5.10E+02
14	44	6.35E+01
16	10	2.87E+00
18	5.2	6.90E-01
20	0.7	1.13E-02

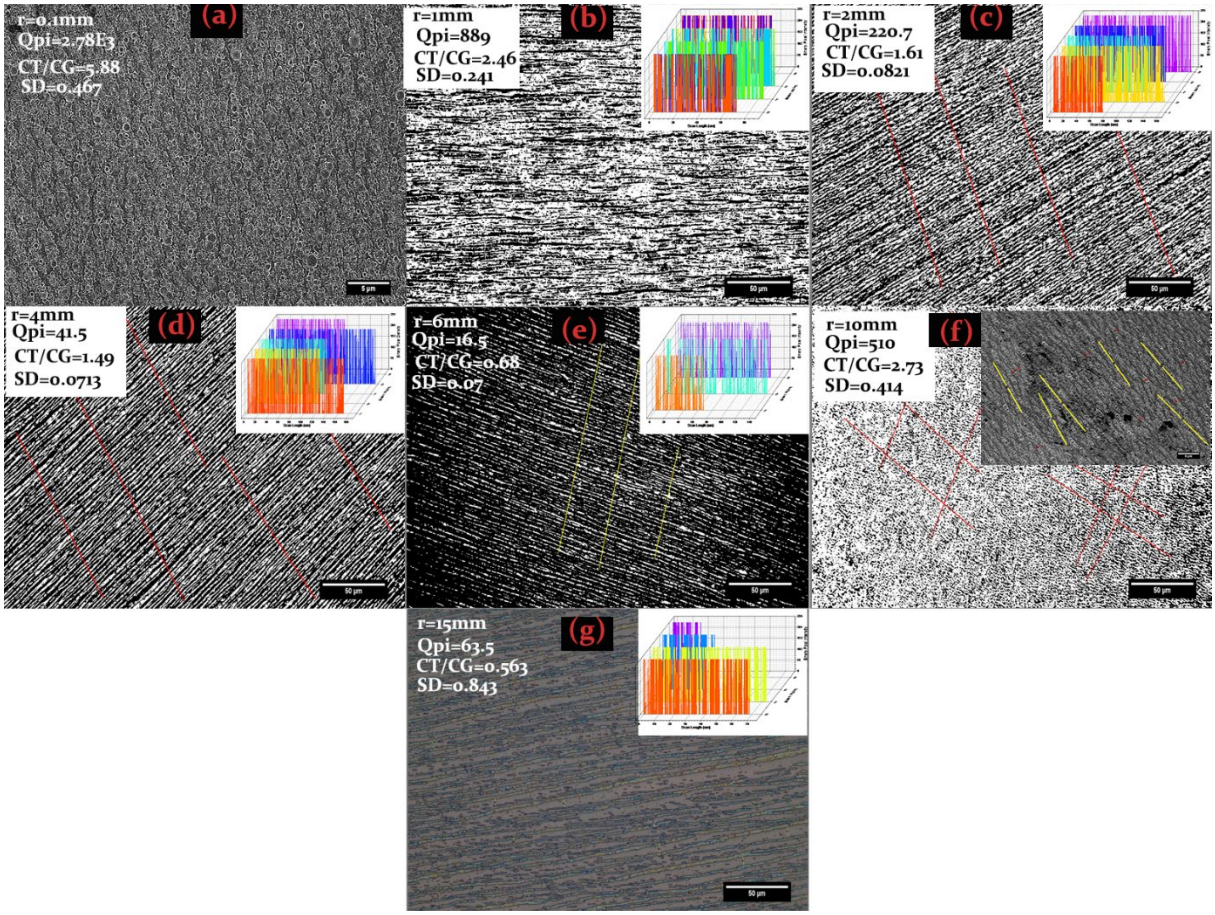

Figure S-5: Thin film nanostructure profile on silicon wafer (a) SEM image 0.1mm close to the centre of the substrate, (b)Binary image 1mm from the centre of the substrate with binarized plot profile of resolution, (c) Binary image 2mm from centre of substrate with binarized plot profile of resolution, (d) Binary image, 4mm from middle of substrate with binarized plot profile of resolution, (e) Binary image, 6mm from middle of substrate with binarized plot profile of resolution, (f) Binary image, 10mm from centre of substrate with SEM image insert and measurements, (g) Binary image, 15mm from centre of substrate with binarized plot profile of resolution.

S.3) Defectivity

S. 3.5) Single and compound

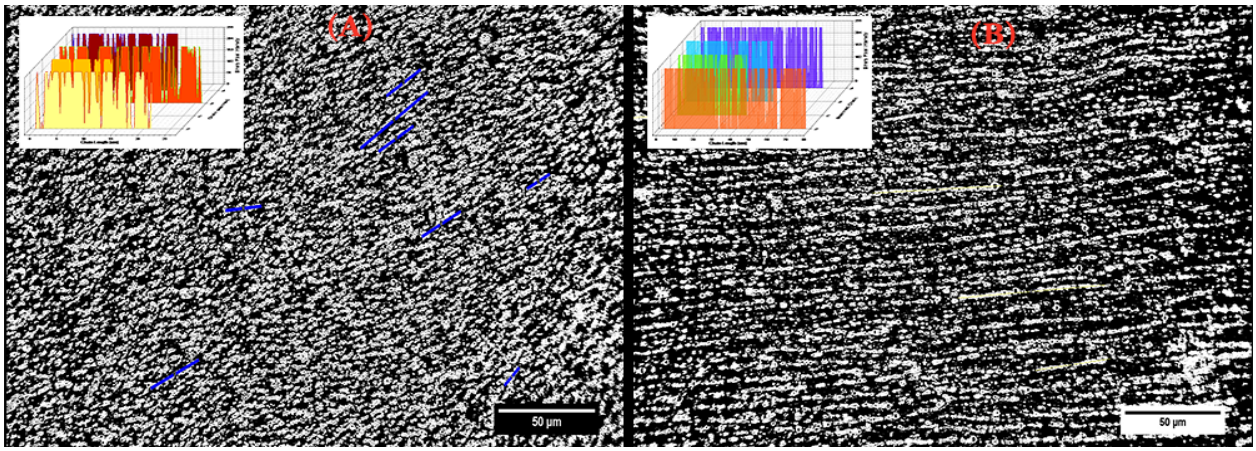

Figure S-6: Defectivity trace detection for (a) QPI = 1.754 and (b) QPI = 0.0302. The inserts are representative 3D plot profiles of 4 scan region of interest lines across varying chain length within each image. (a) tend to have shorter chains but thicker profile bars, while (b) have longer chains but less thicker bars. The defectivity for (a) is 4.3% with SD = 0.0193 and (b) is 11.6% with SD= 0.0285.

Table S-VIII: This is a result summary from image analysis of structured sample estimating its area defectivity from gap between consecutive tail and head of chains along an array and short gaps within individual chains (DEFCL).

Q_{PI}	CL (µm)	Percent gap between head and tail of consecutive chain in an array (% of CM/CL)	Defectivity on individual chain (DEF_{CL})	SD	Final Defectivity DEF_A $DEF_{CL} + \frac{CM}{(CM + CL)}$	SD
112.8	22.1	30.1	-	-	0.231253	0.036
17.5	25.5	20.58	0.043311	0.019	0.214012	0.019
2.28	124	8	0.11625	0.029	0.190324	0.029

S. 3.6) Concentric

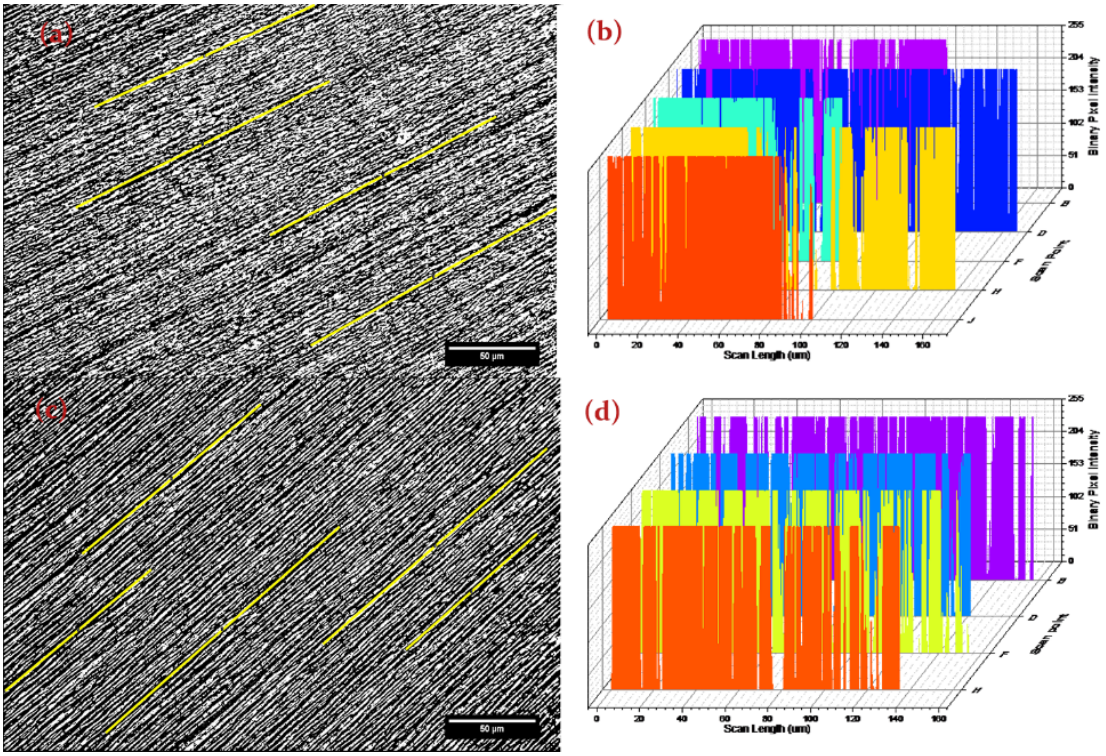

Figure S-7: Defectivity profile measurements of random chains with (a) Qpi = 220.7 and (b) representative binary plot profiles, (c) Qpi = 41.5 and (d) representative binary plot profiles.

Table S-IX: Defectivity determination from Profile scan results from Figure S-5

Qpi	Pixel Count	Droplets pixel counts	Gap pixel counts	CL (um) 0.1677 um/pixel	Defect on Individual profiles	Mean Defectivity	SD
220.7	744	702	42	124.7688	0.056452	0.13	0.0566
	994	895	99	166.6938	0.099598		
	555	471	84	93.0735	0.151351		
	949	752	197	159.1473	0.207587		
	605	524	81	101.4585	0.133884		
41.5	938	830	108	157.3026	0.115139	0.153	0.0315
	843	726	117	141.3711	0.13879		
	924	759	165	154.9548	0.178571		
	804	660	144	134.8308	0.179104		

S. 3.7) Scanning Electron and Transmission Electron Micrographs

The images in this section reveal detailed ferrofluid droplets dipole interaction of heat-treated sample

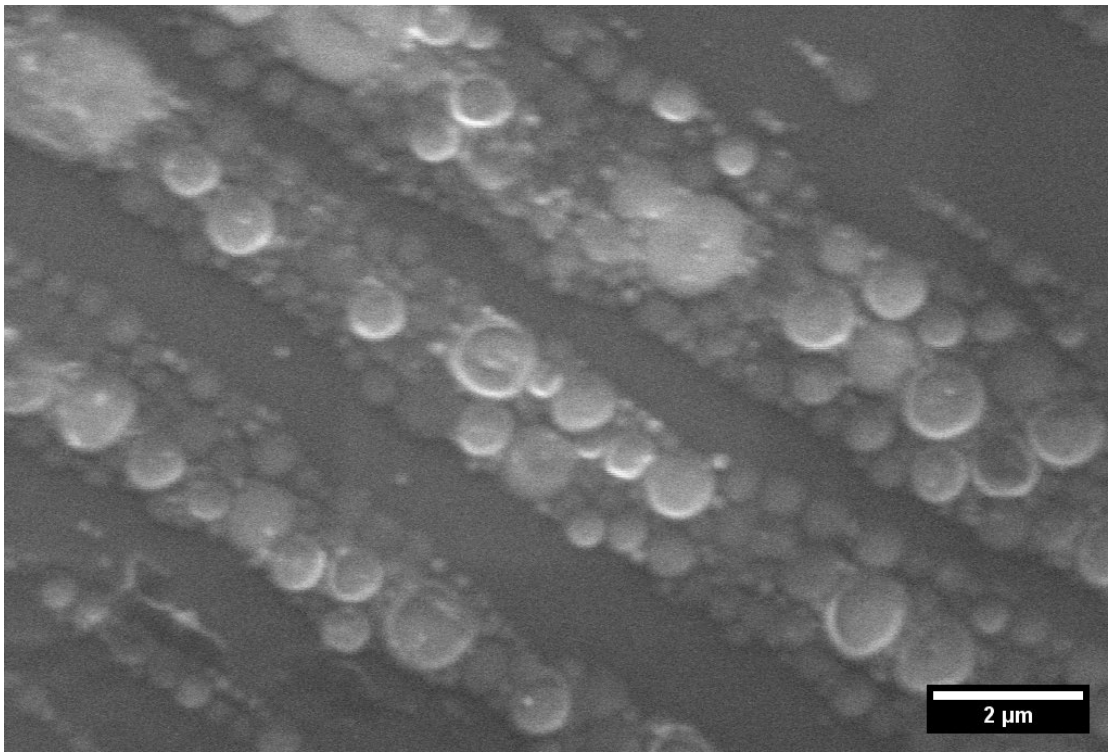

Figure S-8: The enlarged image of the insert in Figure 7b

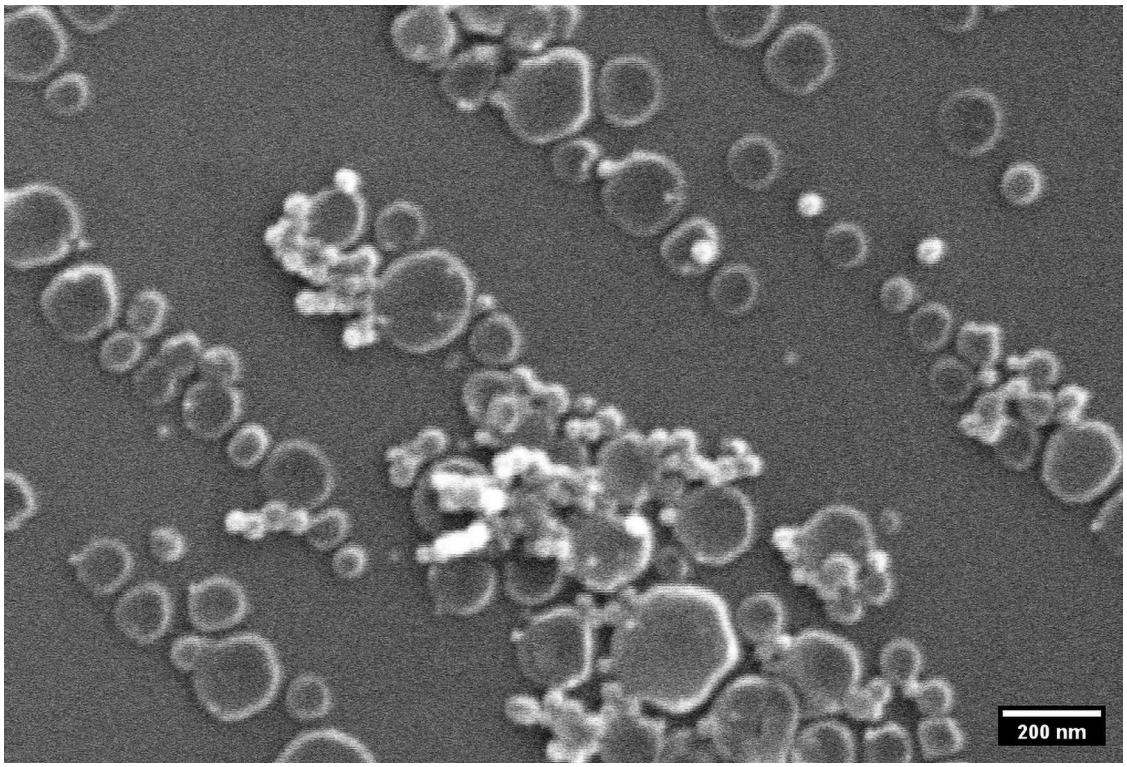

Figure S-9: The elliptical formation of ferrofluid droplet after burning of PVA film from the silicon wafer.

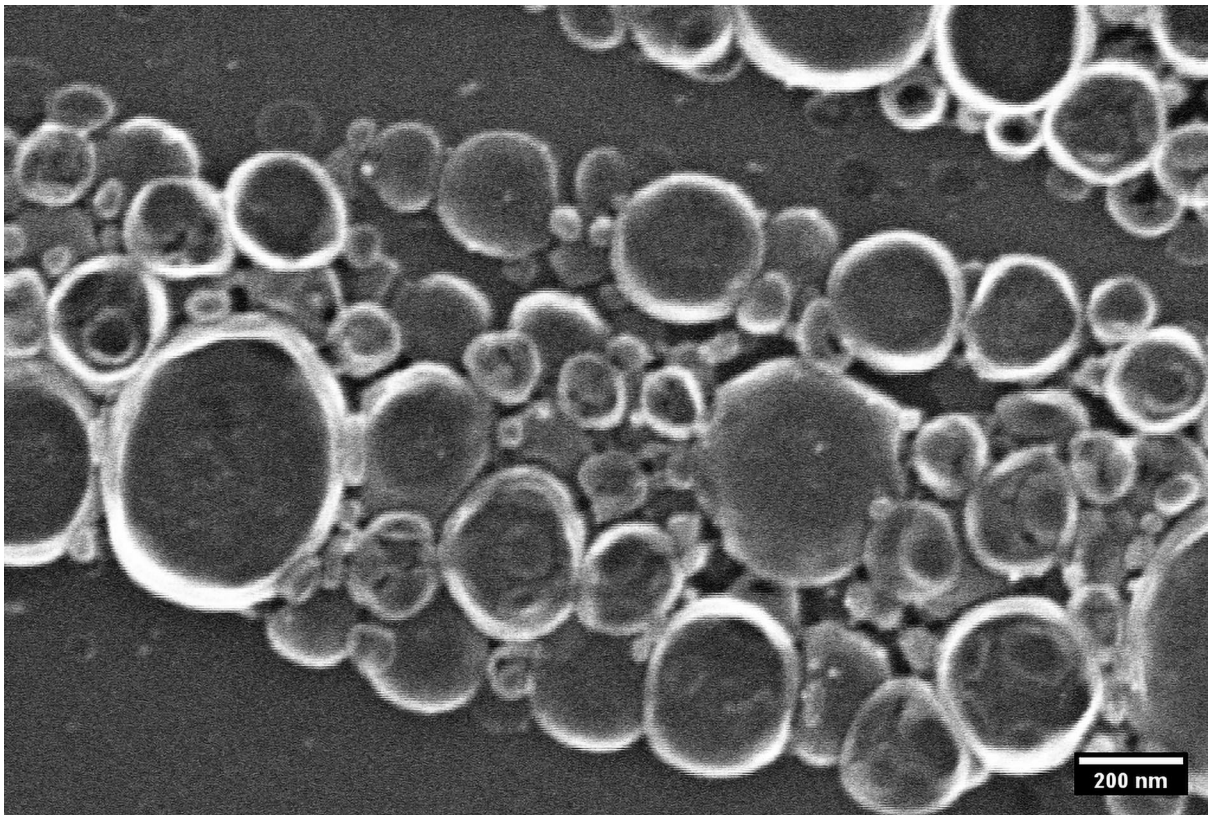

Figure S-10: SEM image of ferrofluid droplet dipole cluster in building approximately 700nm thick chain with gap in between the chains.

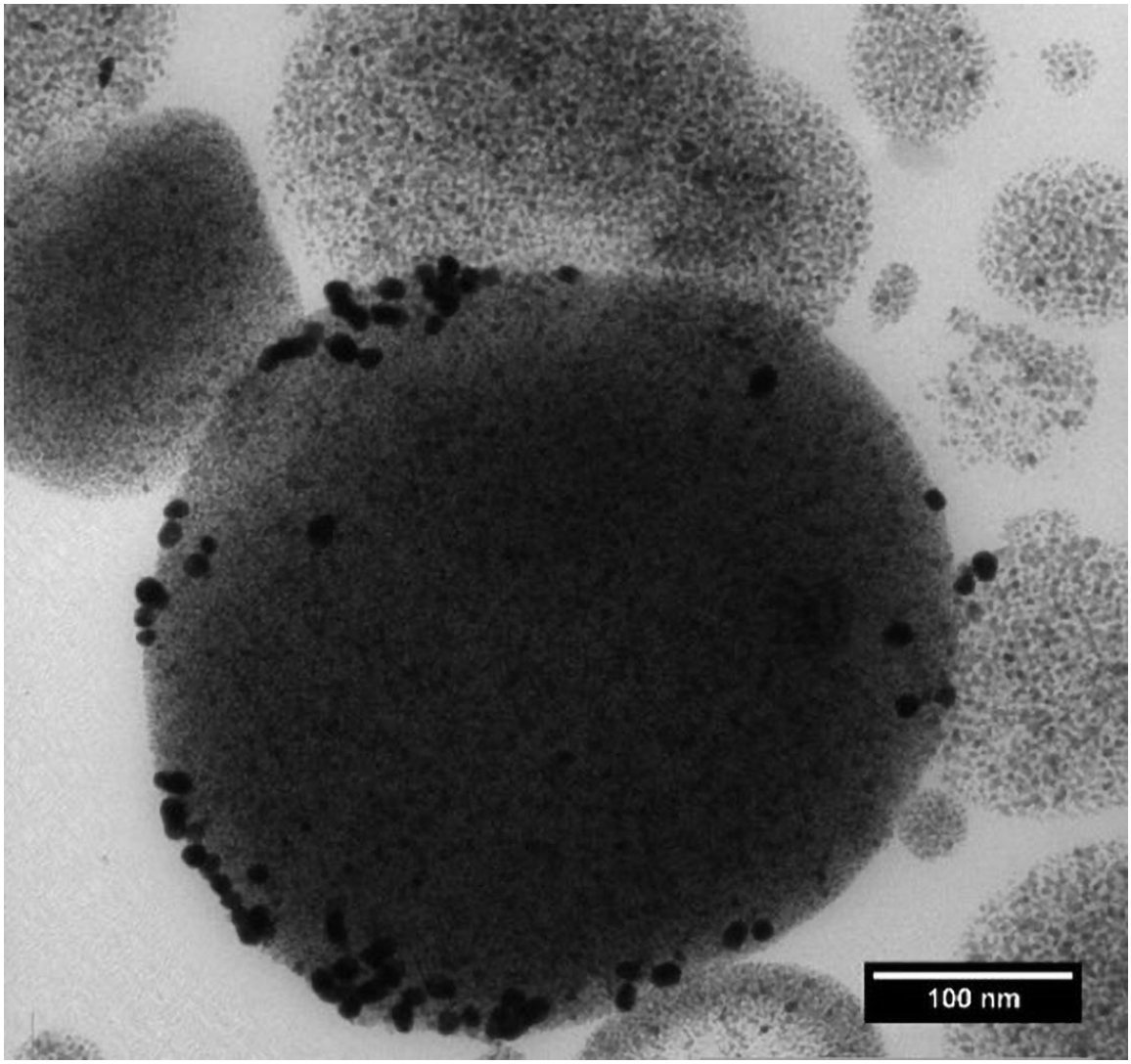

Figure S-11: TEM images of gold pickering ferrofluid droplet (Reproduced from Ref 27 with permission from the Royal Society of Chemistry).